applied sciences

MDPI

Article

HERMES CubeSat Payload Thermal Balance Test and Comparison with Finite Volume Thermal Model

Matteo Quirino [1,*], Giulia Sciarrone [2], Raffaele Piazzolla [3], Fabio Fuschino [4], Yuri Evangelista [3], Gianluca Morgante [4], Manfredo Guilizzoni [5], Luca Marocco [5], Stefano Silvestrini [1], Fabrizio Fiore [6] and Michèle Lavagna [1]

[1] Department of Aerospace Science and Technology, Politecnico di Milano, 20156 Milano, Italy
[2] Department of Mechanical and Aerospace Engineering, Sapienza Università di Roma, 00185 Roma, Italy
[3] National Institute for Astrophysics, 00133 Roma, Italy
[4] National Institute for Astrophysics, 40129 Bologna, Italy
[5] Department of Energy, Politecnico di Milano, 20156 Milano, Italy
[6] National Institute for Astrophysics, 34143 Trieste, Italy
* Correspondence: matteo.quirino@polimi.it

Abstract: Scientific payloads onboard CubeSats usually have complex geometries and occasionally narrower allowed temperature ranges with respect to the rest of the spacecraft. In these cases, the capability to correctly predict the thermal behaviour of the payload once in orbit is mandatory. To achieve this ability, a thermal balance test is required to correctly identify the thermal model of the payload. The test consists in the application of different external thermal boundary conditions together with the addition of heat dissipation to simulate the thermal load produced by active electronics during operation. Those experimental data are fundamental to validate the numerical thermal model and make its predictions reliable. This paper presents the configuration and procedures of the thermal balance test performed on the Demonstration Model of the payload to be embarked on each satellite of the HERMES constellation. The test data is compared with the results of a finite volume thermal model of the payload, proving the application of this method to be reliable for space thermal analyses. The obtained test results show the temperature jumps caused by the heat dissipation applied to active components. A weak correlation between the payload interface and internal equipment has been observed, thus proving that the payload is almost decoupled from the Service Module temperature variations. Based on test outcomes, some modifications in the payload design have been implemented, with the aim to lower the operative temperature on critical, temperature-sensitive equipment.

Keywords: CubeSat; thermal balance test; Gamma Ray detector; OpenFOAM; thermal model

Citation: Quirino, M.; Sciarrone, G.; Piazzolla, R.; Fuschino, F.; Evangelista, Y.; Morgante, G.; Guilizzoni, M.; Marocco, L.; Silvestrini, S.; Fiore, F.; et al. HERMES CubeSat Payload Thermal Balance Test and Comparison with Finite Volume Thermal Model. *Appl. Sci.* **2023**, *13*, 5452. https://doi.org/10.3390/app13095452

Academic Editor: Paride Gullo

Received: 22 March 2023
Revised: 22 April 2023
Accepted: 24 April 2023
Published: 27 April 2023

1. Introduction

The thermal model of a spacecraft is normally exploited to verify that, once in orbit, the onboard equipment operates inside prescribed temperature ranges along each mission phase. On CubeSats, the most critical components are usually batteries and scientific instruments, as they operate in narrower temperature ranges compared to the rest of the hardware.

The scientific payload (PL) on board the High Energy Rapid Modular Ensemble of Satellites (HERMES) 3U CubeSat [1,2] is based on radiation-sensitive detectors that are required to operate within a relatively narrow temperature range, between −35 °C and −5 °C. It is the strictest thermal requirement among all the spacecraft components, and it constitutes the main driver for the thermal design. A detailed numerical thermal model is needed to properly assess the compliance of such requirement prior to the mission launch during detailed design activities. Nevertheless, the correct identification of the model parameters can be achieved only by means of a Thermal Balance Test (TBT) [3]. The test

is performed on a PL Demonstration Model (DM), that is identical to the flight hardware except it has no functional electronics. To mimic the correct heat dissipation, the latter is simulated by electrical heaters strategically placed on locations upon the different boards. This paper presents the procedures adopted to set up and perform the test and discusses the obtained experimental results. Being a CubeSat mission, the full ECSS standard regarding thermal control and thermal testing ECSS-E-ST-31C [3] is partially applicable as reported in CubeSat tailored ECSS [4] but the HERMES team aims at reaching full ECSS standards to provide the best quality of the product.

The currently available literature on CubeSat thermal balance test is very scarce [5,6] and does not explain in a detailed manner the test setup and procedure. The goal of the paper is to provide the reader with all the technical information (e.g., requirements and technical equipment) needed to replicate the test with all the standards tailored from the ECSS. Furthermore, it is the first time the Finite Volume Method is applied for a CubeSat thermal analysis with the level of high geometrical detail reported in the following chapters.

During the design activities of the HERMES mission, a Finite Volume Thermal Model (FVTM) was developed and actively maintained. The FVTM model is computed in OpenFOAM, a widely used open-source Computational Fluid Dynamics (CFD) solver which support also several heat transfer models. The model has a more accurate geometry with respect to the Lumped Parameter Approach method which is commonly used in space thermal analyses, e.g., when simulating with the ESATAN software, the European Space Agency Lumped Parameter Approach software used for thermal analyses; for more information on ESATAN the reader can refer to [7]. Indeed, the FVTM offers better insight into the heat fluxes within the model as shown in [7–9]. In this work, the post-processing of the experimental data is presented, and the test data is compared with the FVTM results, proving the application of the novel method to be reliable. Furthermore, the comparison creates a solid base upon which the method can be applied to other cases in space thermal analyses such as the generation of infrared images as reported in [10–13].

Other results are presented in the article, such as the time needed to reach steady-state, and the temperature jumps caused by the simulated electronics heat dissipation are identified. Furthermore, it has been proven that the internal components of the PL are slightly influenced by the temperature changes at the mechanical interface with the Service Module. In the end, given the thermal behaviour of the PL, planned future updates of the thermal interfaces are presented. Summarizing, the objectives of the paper are:

- to develop a Finite Volume Method for a CubeSat thermal analysis with a high level of geometrical fidelity;
- to identify critical geometries that play fundamental roles in the thermal behaviour of the HERMES payload;
- to design, set up and execute a thermal test for the HERMES payload, providing all the details for the equipment and procedures to provide a baseline for any reader that has no experience with such type of test.

2. The HERMES Pathfinder Mission

2.1. Overview

The HERMES programme [1,2,14–18] envisages a constellation of six CubeSats as pathfinders for the observation of high energy transient events, such as Gamma Ray Bursts (GRBs) through a set of distributed sensors, three of them supported by the Agenzia Spaziale Italiana—through the HERMES Technological Pathfinder project—the last three financed by a H2020 European Commission study—named HERMES Scientific Pathfinder. In particular, the mission aims at demonstrating the feasibility of reconstructing the position of GRBs by means of triangulation across different satellites, exploiting the time delay of the same event detected by different elements of the constellation. The constellation is planned to be launched in 2023 on circular nearly-equatorial orbits at 550 km of altitude. Once in flight, the nanosatellites will naturally drift apart due to orbital perturbations, quickly reaching a relative baseline distance sufficient to perform GRB triangulation [14,15].

For more details on the triangulation procedure the reader can refer to [19] whilst for details about the constellation orbital drift and mission analysis more information can be retrieved in [14,15].

All HERMES CubeSats are equipped with an Iridium transceiver that enables a fast link to the ground through the Iridium constellation, deployed at 780 km of altitude [1]. As soon as the PL on board each satellite detects a GRB, an alarm signal is transmitted to the ground and broadcast worldwide to astronomical observatories to enable complementary scientific observations. An overview of the satellite configuration is shown in Figure 1. The HERMES satellite consists in a three-unit CubeSat: the top unit hosts the scientific payload (Figure 1c), while the other two units constitute the Service Module (SM) (Figure 1d). The overall envelope is 10 × 10 × 30 cm. The payload occupies 1U, meaning 10 × 10 × 10 cm.

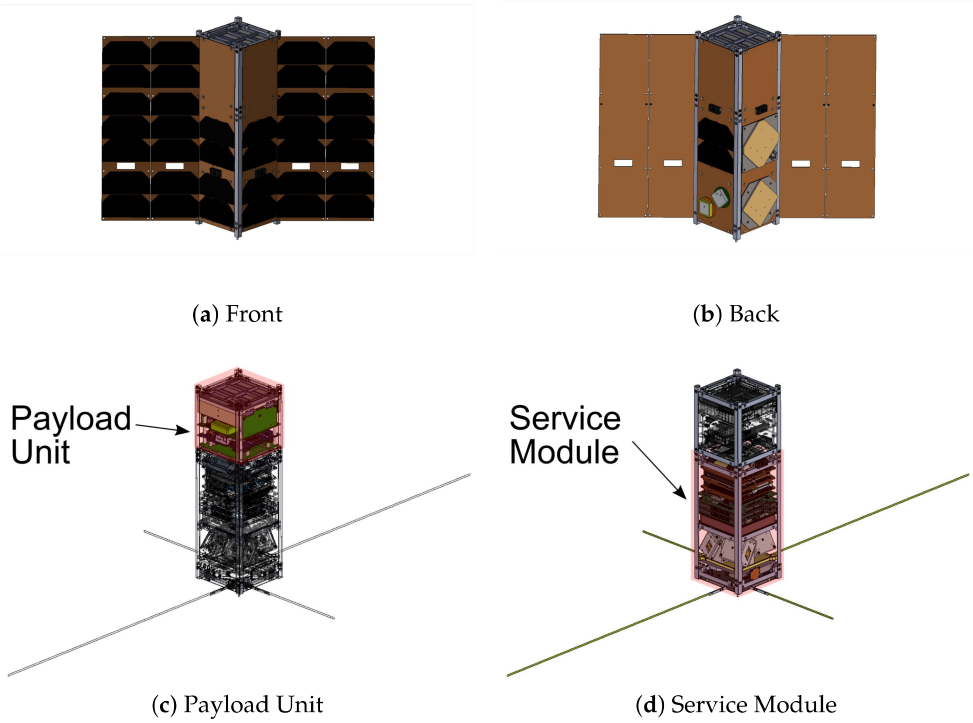

(**a**) Front (**b**) Back

(**c**) Payload Unit (**d**) Service Module

Figure 1. HERMES CubeSat.

2.2. Scientific Payload

The HERMES Scientific Payload was designed by the Istituto Nazionale di Astrofisica (INAF) and has the task of performing high resolution spectral-timing analysis of long and short GRBs [20–27]. Whenever a GRB is detected, the estimated location of the CubeSat and the timestamp of the detection are saved in order to triangulate the GRB direction with an accuracy of several degrees (depending on the nature of the GRB and the configuration of the triplet observing the event). The time accuracy is provided by a chip-scale atomic clock integrated in the PL which is maintained synchronized with the GPS time via PPS synchronization. To ensure the atomic clock timing accuracy, the component temperature must be kept above −10 °C [28]. For what concerns GRB detection and energy time history recording, the PL relies on 120 Silicon Drift Detectors (SDDs) and 60 GAGG crystals, with each crystal coupled with two SDDs. More details on the high energy transient detection can be found in [21]. SDDs constitute the core of the instrument, and they are required to operate below −5 °C to limit the amount of leakage current due to on-orbit radiation damage, guaranteeing the instrument spectroscopic performance and the required lifetime. In order to keep such low temperatures, the PL structural panels act as a selective surface thanks to an Aeroglaze coating [29] that reflects the majority of the sunlight and maximizes the radiative heat flux emission in the infrared spectrum. Figures 2 and 3 show the

breakdown of the PL internal components and the associated nomenclature, adopted to identify the PL subsystems in the remainder of the paper.

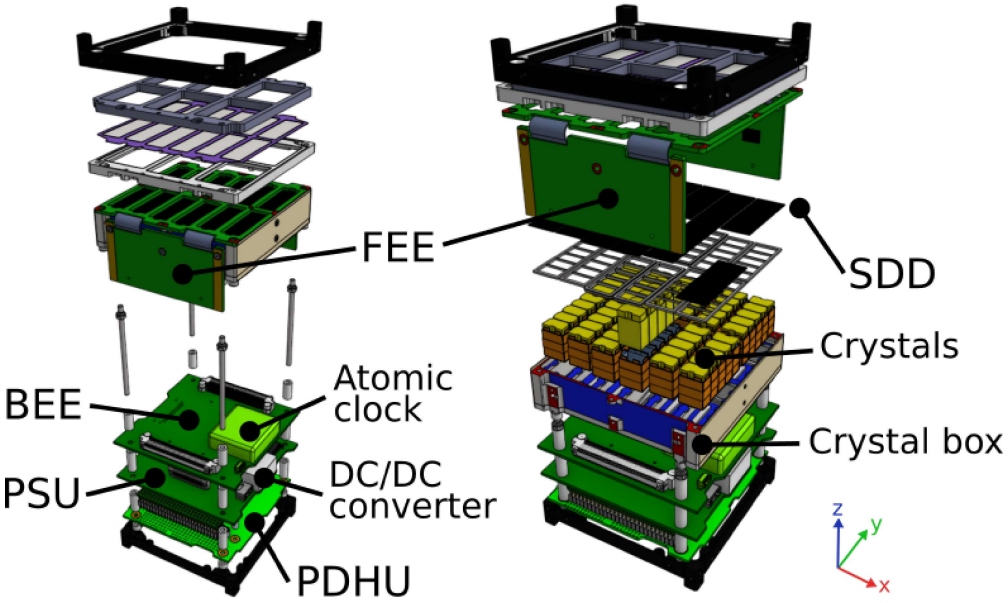

Figure 2. HERMES scientific payload insight. Electronics (**left**) and detector (**right**).

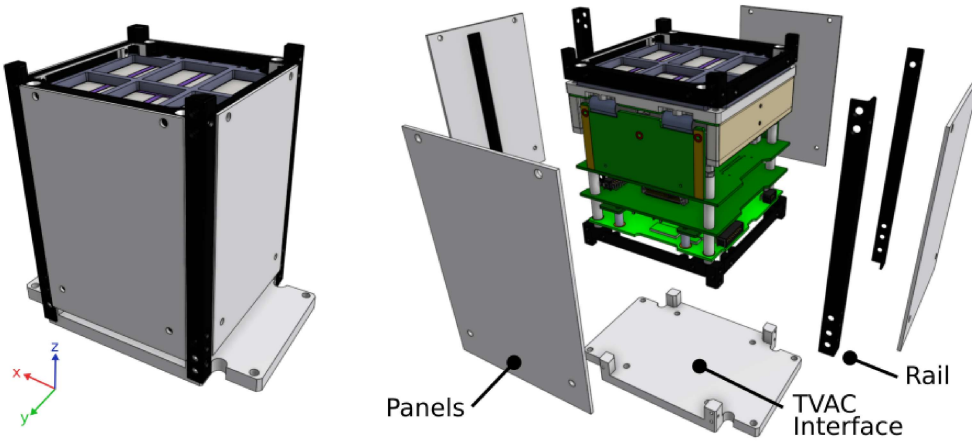

Figure 3. HERMES DM with TVAC interface. TVAC interface on bottom right.

2.3. Demonstration Model

Given the complex geometry of the PL and its strict operative temperature requirements, the correspondence between the numerical thermal model and the thermal behavior of the actual equipment shall be ensured by proper model parameter identification. The only way to achieve such confirmation is to perform a TBT using a Thermal Vacuum Chamber (TVAC) [3]. The goal of the TBT is to allow a PL model to reach different thermal steady-state conditions in a vacuum environment in order to observe the thermal behaviour of the system in response to different imposed boundary conditions. The Demonstration Model (DM) of the payload adopted for this purpose is fully representative of the Flight Model (FM) from a thermo-structural point of view, except it has no functional hardware, meaning that some electronics boards cannot be switched on to perform functional tests. Heat dissipation by electronics plays a major role in the determination of the system operative temperature and cannot be neglected: electric heaters are placed on the active components to impose the required thermal flux (more details on that are given in Section 3.2). Heaters are fundamental in order to assess how the electronics heat dissipation

affects the temperature fields of the PL. In particular, it is crucial to see how such heat dissipation affects the temperature of the SDDs. Indeed, in the DM, the SDDs, the crystals and the boards are arranged as in the flight configuration, thus all the conductive paths connecting the detectors with the electronics are identical to the actual PL (more details on the connections are given in Section 3.2 and in [20–22]). The DM also differs from the flight model because the atomic clock and the high-voltage DC/DC converter are absent, replaced with equivalent mass brass dummies (more details in Section 3.2).

3. Test Procedures

3.1. TVAC Overview

The test was carried out in the TVAC located at the Experimental Test Laboratory of the Department of Aerospace Science and Technology of Politecnico di Milano. Figure 4 offers an overview of the facility overview: the chamber is a steel cylinder with a diameter of 1 m, 1.2 m long, 5 mm thick, for an effective volume of 0.9 m^3. Inside, an aluminum cold plate—800 mm × 630 mm × 15 mm size—is located in the bottom part, as shown in Figure 4b. The plate can be heated up to 200 °C due to the six embedded resistors, powered at 350 W each. The resistors are controlled with a Gefran 1600 PID controller that can keep the plate temperature within ±1 °C from the set point whenever the controller feedback thermocouple is placed on the plate. The base plate is also connected to the fluid cooling system through a serpentine attached underneath, as shown in Figure 4c. The cooling system is composed of two independent single-stage refrigeration systems, that can lower the temperature of the plate to −75 °C. For more information on the cooling and heating systems of the chamber, the reader is invited to read [30–33].

The cooling system is controlled by a second Gefran controller that operates in relay mode, i.e., it keeps switching on and off the cooling system in order to reach the set point temperature. This peculiar control policy is more subject to inaccuracies: when cooled, the plate temperature can undershoot the set point up to −10 °C. This behaviour is well known and documented [30], and it has to be compensated during the TVAC operations.

Above the plate there is a shroud (Figure 4b) connected to the cooling system, which can be operated independently with regard to the base plate (Figure 4d). In addition, six infrared lamps of 1 kW each are equally distributed on the upper part of the shroud as shown in Figure 4b. As explained in Section 3.2, the shroud cooling systems and the lamps are not activated during the test.

A high vacuum inside the chamber is achieved by a dual stage pumping system [30]: the first stage brings the pressure down to 1×10^{-3} mbar; passed this threshold, the second stage (i.e., a turbomolecular pump) is activated and the pressure can be dropped to 1×10^{-6} mbar which satisfies the ECSS maximum pressure requirement for thermal vacuum test of 1×10^{-5} mbar [34].

3.2. Test Configuration

This section describes the PL test preparation. Due to its configuration, the PL needs to be integrated "upside down" with the SDD and crystals facing downward, as shown in Figure 5. During this process, the electronics support boards of the detector, namely, the FEE lateral boards, are disconnected from the back end electronic board BEE and kept in place by two integration supports, shown in Figure 5a. For more information on the PL boards the reader can refer to [20,21]. The temperature sensors, used in the TVAC test to monitor the PL, are placed during the DM integration phase. A thermocouple (TC) is fixed at the bottom of the crystal box (Figure 5b) while a second thermal sensor is placed on the FEE lateral wing as shown in Figure 5c. As the FEE wings are the main heating path toward the SDDs, the latter TC is included to monitor the heat flow toward the most sensitive part of the assembly, with the aim to obtain a finer estimation of the thermal interfaces, needed to refine the design and to further limit the heat flow to the SDDs. Type T thermocouples (https://it.rs-online.com/web/p/termocoppie/3630266 (accessed on 2 November 2022)), produced by RS and with an accuracy of ±1 °C have been adopted for this test. Each TC is

fastened with one layer 0.127 mm thick Kapton tape and covered with aluminum tape to provide shielding from infrared radiation [35]. The list of the thermocouples adopted in the test campaign, together with the relative nomenclature and the references to correspondent figures is summarized at the end of this section.

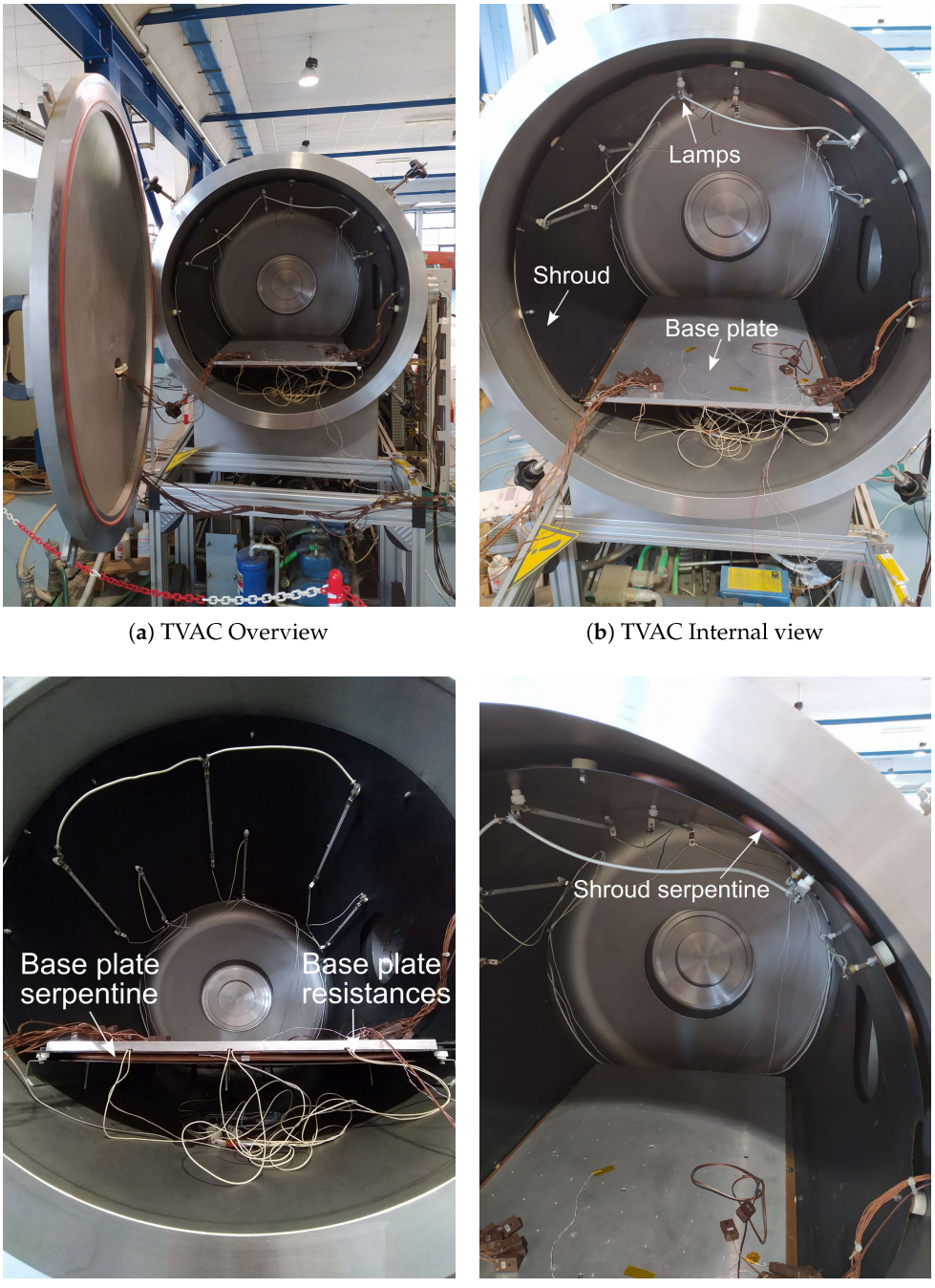

(**a**) TVAC Overview

(**b**) TVAC Internal view

(**c**) TVAC Base plate serpentine

(**d**) TVAC Shroud serpentine

Figure 4. TVAC main components.

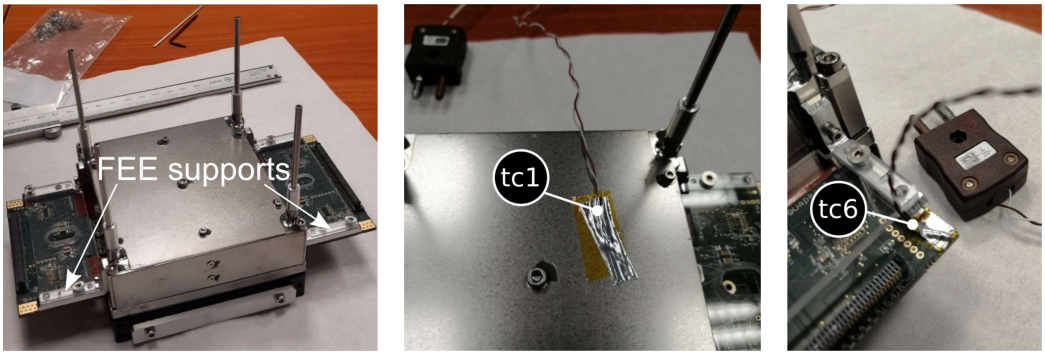

(**a**) FEE supports (**b**) Crystalbox thermocouple (**c**) FEE thermocouple

Figure 5. FEE and crystal box thermocouples.

Heaters are mounted on the BEE and PSU before their integration to provide the correct heat dissipation. The model of the heaters is Arcol HS10 (http://www.arcolresistors.com/resistors/hs10-aluminium-housed-resiso/ (accessed on 2 November 2022)), compliant to both Military (MIL) and International Electronic Commission (IEC) standards. They are strategically placed on electronics to reproduce heat generation due to specific active components actually not functional in the PL Demonstration Model: a heater is mounted on the BEE, in place of the FPGA (Figure 6a); a second heater is located on the PSU on the dummy DC/DC converter (Figure 6b), and a third is placed on the PDHU [36] on the SD card slots (Figure 6c).

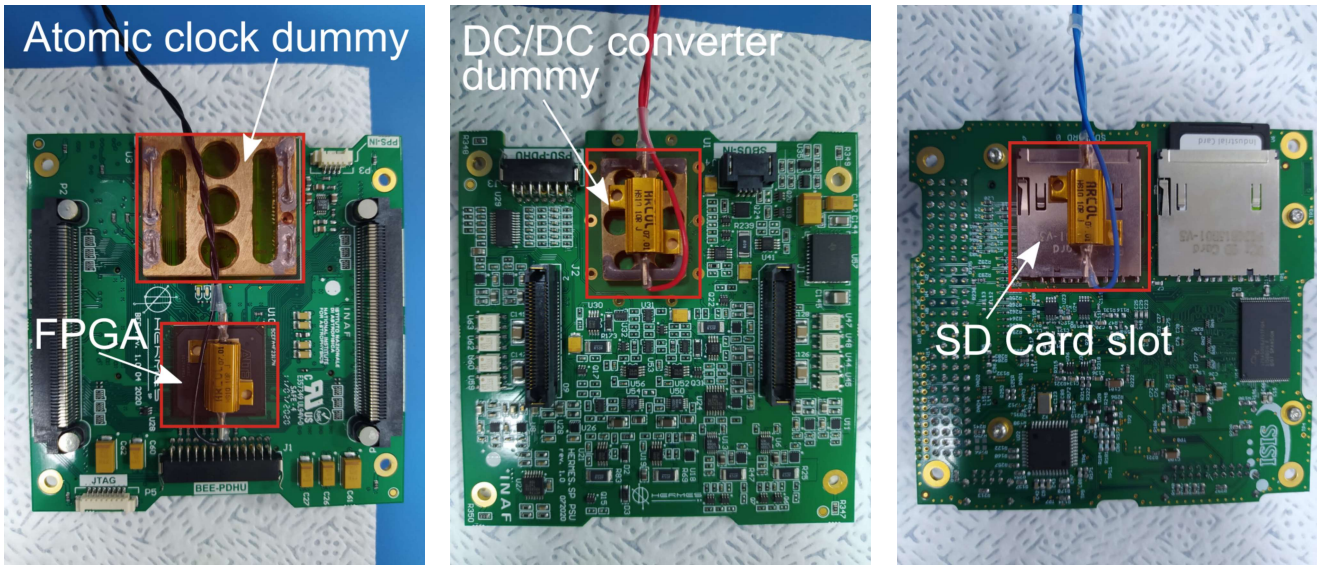

(**a**) BEE heater on FPGA (**b**) PSU heater on DC/DC converter (**c**) PDHU heater on SD slot

Figure 6. Heaters positions. Heaters are the ones connected with wires in the pictures.

Heaters are held in place by an adhesive film plus one layer 0.127 mm thick Kapton tape strip. A TC is placed close to each heater to directly monitor its temperature. TC positions near the heaters are shown in Figure 7a for the BEE-PCB and in Figure 7b for the PSU-PCB.

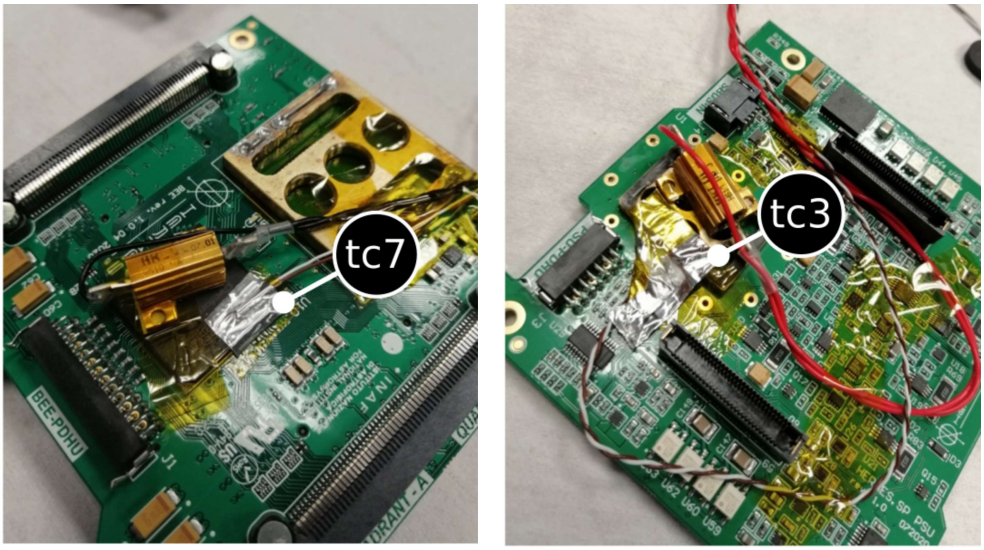

(**a**) TC near BEE FPGA (**b**) TC near PSU DC/DC converter

Figure 7. TCs on BEE and PSU PCBs.

At this point, the PL integration is completed by removing the FEE integration supports, leaving the wings free to be folded along the lateral faces. The remaining electronics are inserted in position, and the bottom structural rib is locked to hold the full stack in place (Figure 8a). Wires are routed between the PDHU-PCB (i.e., the PCB at the bottom of the PL) and the structural rib (Figure 8b), thus the last heater is placed on the PDHU-PCB with the respective TC, as shown in Figure 8c. As last step, payload side panels are integrated, and the assembly is connected with the mechanical support that provides the correct interface with the TVAC cold plate. Two thermocouples are located on the interface, as shown in Figure 9a: one of them is selected as reference for the TVAC controller, enabling direct control of the PL thermal interface, while the second is used for monitoring purposes. The recording of the temperature at this point is of particular importance, as it represents the main thermal interface between scientific payload and Service Module.

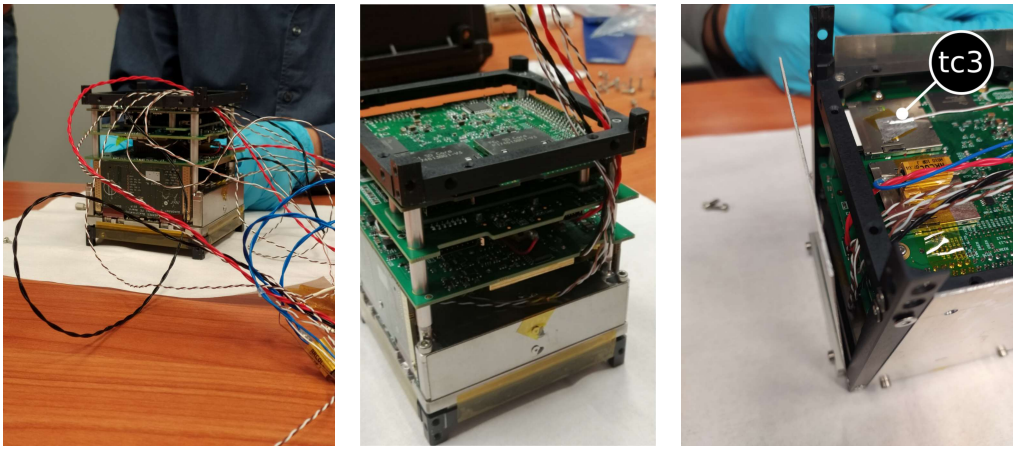

(**a**) Wires routing (**b**) Wire routing zoom (**c**) TC on PDHU SD Card

Figure 8. Routing of all the wires connecting TCs and heaters.

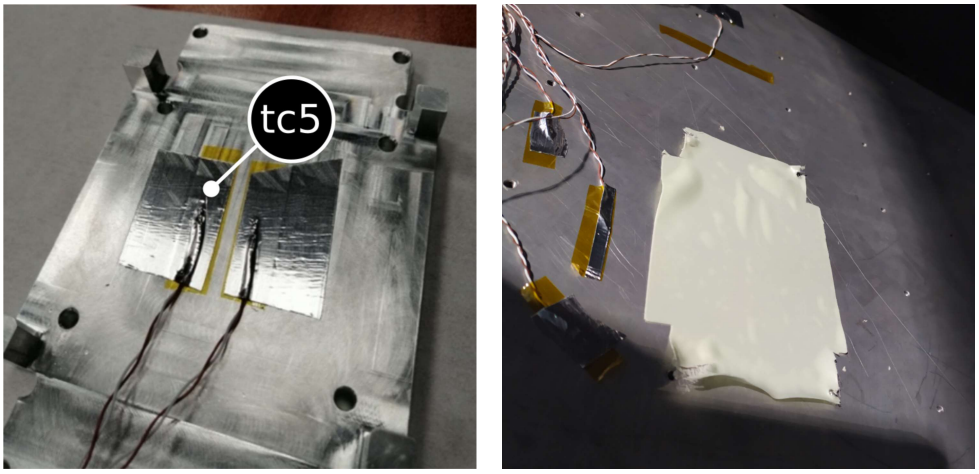

(**a**) TC on TVAC interface (**b**) Thermal pad (picture taken end of test)

Figure 9. Thermal pad and TC at TVAC interface.

The payload is integrated with the mechanical interface support; a conductive pad (Laird TFlex 340 (https://www.laird.com/products/gap-fillers-thermal-interface-materials/gap-fillers/tflex-300/a15324-02 (accessed on 2 November 2022))) is applied below the interface to maximize the heat flow between the TVAC cold plate and the payload assembly (Figure 9b). After the pad application, the whole assembly is fixed to the TVAC base plate by means of four M4 screws, installed with a 2 N m tightening torque. At the end, TCs on the lateral panels, structure and base plate are applied as shown in Figure 10.

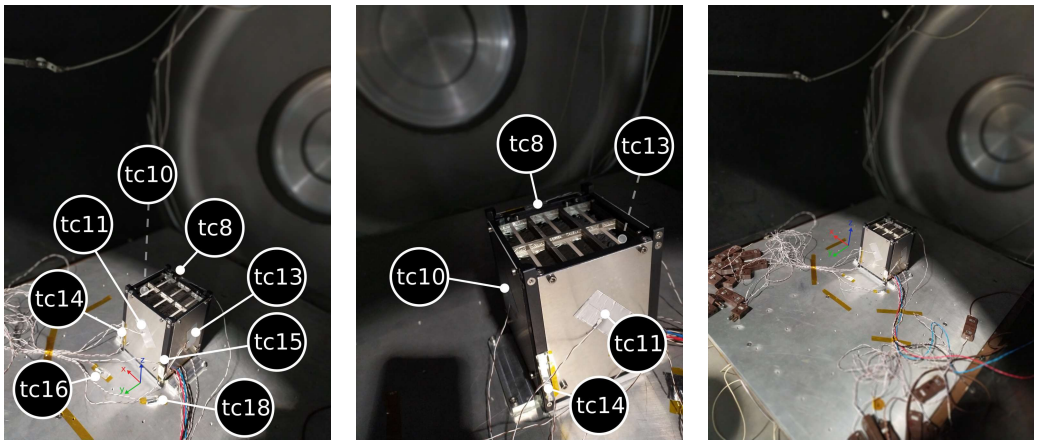

(**a**) TCs on the structure (**b**) TCs on the structure (**c**) TCs and heaters plugged

Figure 10. TCs on structural components. DM is fixed with the TVAC baseplate.

The last preparation step consisted of the aluminum radiation shield (1 mm thickness foils) placement all around the PL (Figure 11a). The shield just lays on the TVAC base plate and it is correctly centred around the DM using reference marks on the base plate. Its role is to provide a simple and easily reproducible thermal radiation environment around the specimen as the dimensions and inner infrared emissivity of the shield are known. Measurable and easy-to-reproduce boundary conditions (BCs) are mandatory to replicate the whole test in a numerical simulation, needed to properly correlate the thermal model with the test results.

In the absence of a thermal shield, BCs would be moved to the TVAC walls (i.e., base plate, hatch, shroud and face opposite to the hatch). In that case, the entire TVAC geometry should be numerically modelled to correctly simulate the radiative test environment. Furthermore, the infrared emissivity of the TVAC walls should be known as well to correctly

model radiation fluxes. Since such data was unavailable, the adoption of a radiation shield solved all the aforementioned uncertainties.

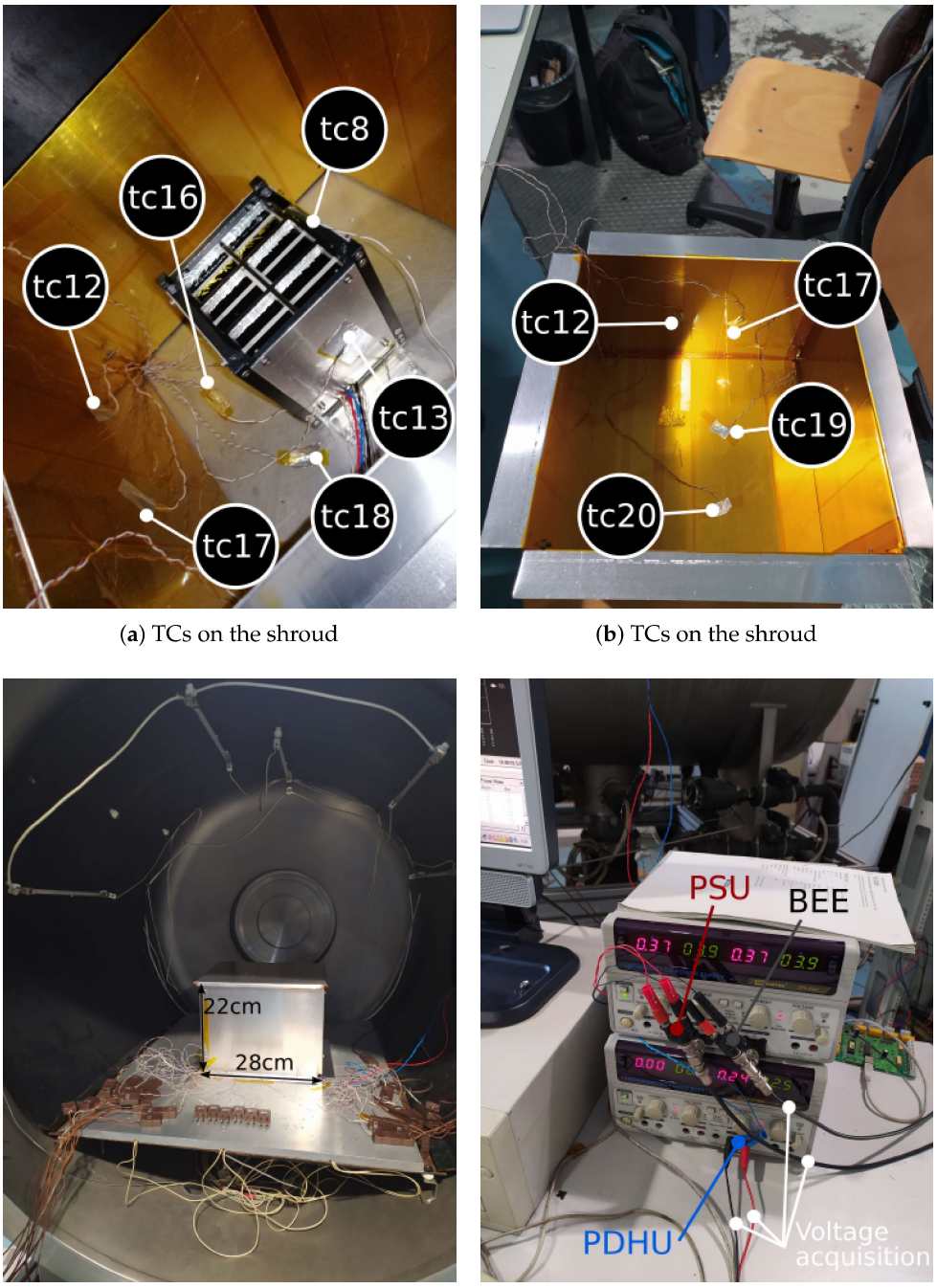

(**a**) TCs on the shroud

(**b**) TCs on the shroud

(**c**) Shroud placed on DM

(**d**) Power suppliers

Figure 11. TCs on shroud and power suppliers.

The interior of the shield is covered with one layer of 0.127 mm thick Kapton tape whose emissivity in the infrared range is known with accuracy. The orange-colored Kapton layers stripes applied on the interior of the shield are well visible in Figure 11a,b. The geometry is much smaller and simpler with respect to the entire chamber: the setup of the numerical simulation is eased, and the computational burden is relieved, for the number of discretized view factors to compute between the DM and the shield is reduced.

Please note that the shield is not fixed to the base plate, but given the small thickness of the aluminium foils and given its small mass, it is not expected to heavily impact the time needed to reach steady-state.

Due to the lack of TCs channels available and due to the configuration symmetry of the payload, TCs are placed just on one side of the shield, assuming that symmetrical faces experience the same temperature. Dedicated TCs have been placed on the top cover, as shown in Figure 11b, since the part is not bolted to the lateral walls, and due to the fact that the PL is not symmetrical in the Z direction. The assumption made for the radiation shield is confirmed by the fact that the side panel and top panel have almost the same temperature as reported in the top graph of Figure 12.

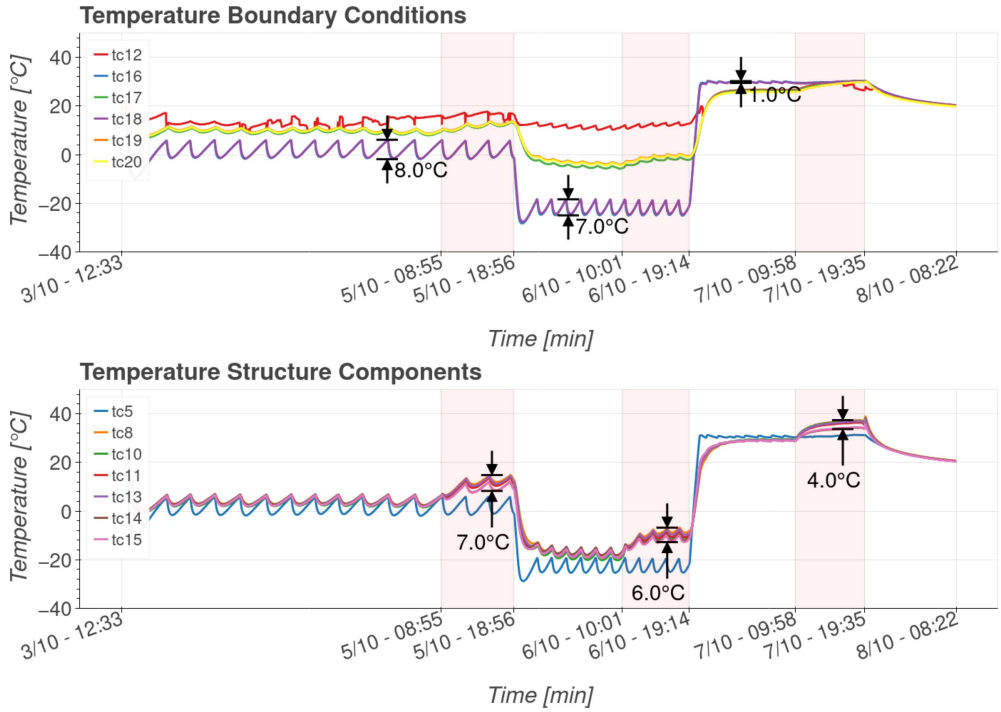

Figure 12. (**Top**) Radiation shield panels and base plate temperatures, (**Bottom**) temperature of structural components. Inside the pale red bands heaters are on.

The proper measure of the BCs is critical for a correct model correlation. For this reason, measures at each boundary point have been acquired by two TCs for the sake of redundancy.

Once the shield is placed (Figure 11c), all thermocouples are plugged to the TVAC feedthrough connectors. The same goes for the heaters by means of a dedicated D-SUB 50 pin connector at the TVAC interface. Heaters are connected to three different channels with 2 GPS-43043 power supplies (https://it.farnell.com/gw-instek/gps-4303/alimentazione-4-o-p-3a-30v-reg/dp/2748523 (accessed on 2 November 2022)) which are manually set and limited in current. Whenever requested, the power supply is turned on with the values reported in Table 1, and Figure 11d.

Table 1. Heaters settings.

Channel ID	Component	Wire Color	Voltage [V]	Current [A]	Power [W]
pch1	PSU	Red	3.9	0.37	1.44
pch2	BEE	Black	3.9	0.37	1.44
pch3	PDHU	Blue	2.5	0.24	0.60

All TCs used and their positions are reported in Table 2.

Table 2. Thermocouples list.

TC	Component	Position
tc1	Cristal Box	Figure 5b
tc3	PSU-PCB	Figure 7b
tc5	TVAC Interface	Figure 9a
tc6	FEE-PCB	Figure 5c
tc7	BEE-PCB FPGA	Figure 5c
tc8	Rib +z −y	Figure 10a
tc9	PDHU-PCB	Figure 8c
tc10	+x Panel	Figure 10b
tc11	+y Panel	Figure 10a
tc12	+y Shroud panel 1	Figure 11a
tc13	−x Panel	Figure 10a
tc14	Rail +y +x	Figure 10a
tc15	Rail +y −x	Figure 10a
tc16	TVAC Base Plate 1	Figure 10a
tc17	+y Shroud panel 2	Figure 11a
tc18	TVAC Base Plate 2	Figure 10a
tc19	Top shroud 1	Figure 11b
tc20	Top shroud 2	Figure 11b

Data Acquisition

TCs temperatures are acquired through an Agilent-34970A Data Acquisition Unit (https://it.farnell.com/keysight-technologies/34970a/data-acquisition-250-ch-sec-22/dp/1335867 (accessed on 2 November 2022)). A 1 min sampling time has been adopted in the tests for both temperatures and voltages applied to the heaters. The voltage is extracted at the output of each power supply, as shown in Figure 11d, and acquired through a general I/O board (National Instruments USB-6289 (https://www.ni.com/it-it/support/model.usb-6289.html (accessed on 2 November 2022))). Table 3 reports all equipment used for the test.

Table 3. Test equipment list.

Entity	Equipment	Number
Temperature sensor	RS PRO Type T [37]	19
Temperature acquisition	Agilent 34970A [38]	1
Heater	Arcol HS10 [39]	3
Heater power supply	GW Instek GPS-43043 [40]	2
Heater voltage acquistion	National Instruments USB-6289 [41]	1

3.3. Test Procedure

The first step in the test procedure is to close the hatch and create a vacuum. The two stage pumping system is activated and kept on for the whole duration of the test. As the pressure stabilizes at 3.5×10^{-6} mbar, the TVAC temperature control can be activated. The temperature at the interface between the payload and TVAC is imposed for three different set points: for each set point of the TVAC control, once steady-state is reached, the heaters are switched on and are kept active until steady-state is reached again. The voltage and current values of the heaters when switched on are reported in Table 1.

ECSS does not impose constraints on the time gradient value for steady-state declaration [3]. Therefore, to avoid waiting more than one day for steady-state and due to oscillation in the cold temperature control of the TVAC, steady-state condition is declared reached whenever the mean of the time temperature gradient of the reference TC over 3 h stays below 0.01 °C min^{-1} for at least one hour. Such value enabled confirming steady-state in 10 h, thus providing a test duration of 3 days for three set points. This assured the respect of the strict timetable of the inspection after the thermal test, imposed by scheduling constraints.

The reference TC used to declare steady-state is tc1, located on the crystal box which is the most massive component of the payload, thus the one with highest thermal inertia: if

such a component reaches steady-state it is reasonable to assume that also the temperature of all components is steady as well. In any case the steady-state condition is verified by the operator on the other components too, before moving to the next test phase.

Due to laboratory access limited to working hours, a longer duration for the steady-state at the first set point was scheduled, as evident in all dates presented in Section 4. Test conditions and ECSS requirements are reported in Table 4.

Table 4. ECSS requirements and test conditions achieved.

Entity	ECSS req	Value	Achieved
Set Point 1	-	-	0 °C
Set Point 2	-	-	−25 °C
Set Point 3	-	-	30 °C
Slew rate crystals	-	-	$\leq$1 °C min^{-1}
Max Pressure	ECSS-E-ST-10-03C—5.5.4.2 [34]	1×10^{-5} hPa	1×10^{-6} hPa
Temperature accuracy	ECSS-E-ST-10-03C—4.4.3 [34]	$\pm$2 K	$\pm$1 K
Steady-state	ECSS-E-ST-31C—4.5.3.2 [3]	-	$\leq$0.01 °C min^{-1}

4. Test Results

The data acquired during the test and the related post processing are presented in this section. It is here remarked that faded red stripes in graphs of the current section mark the time windows in which the heaters were switched on. The first graph reported in Figure 12 shows the actual performance of the TVAC control. It can be observed how the 0 °C set point was initially undershot by 10 °C and during the plateau it keeps oscillating with an amplitude of 8 °C (peak-to-peak) due to the relay controller explained in Section 3.3. Nonetheless, the hot control of the base plate is keeping the oscillations within 1 °C. The same plot highlights that one of the two TCs placed on the external radiation shield registered incorrect results. Indeed, tc12 shows erratic behaviour in disagreement with tc17 placed on the same component (more on that will be added in the next paragraphs).

The bottom graph in Figure 12 (figure time format day/month-hour) shows how all the TCs placed on structural components registered temperatures close to each other within a 7 °C range. That means the structure components of the DM have good thermal conduction links among themselves and the heat flow coming from the baseplate is properly transferred among them. Thus the structure can be used as thermal sink in case of necessity as it is expected that the heat power discharged on it will be distributed in a uniform way without creating big temperature gradients.

The bottom graph of Figure 13 reports the heaters power history whilst their effect on the boards on which they were placed can be easily noticed in the upper graph of the same figure. The power history graph reveals that the power channel pch1, delivered on the PSU-PCB, oscillates: that is most probably due to electrical resistance changes caused by temperature variations in the materials at the set points. Indeed, during the test the power generators switched from current limited control to voltage control. Whenever in voltage control configuration, the power supply is free to change the current value, that is not registered; thus during those oscillations the power values reported in the graph are not reliable. This is due to the fact that the power is computed by multiplying the registered voltage measures times the current values fixed at the beginning of the test and assumed constant. Nonetheless, oscillations are contained and the effect of the resistance variations can be neglected.

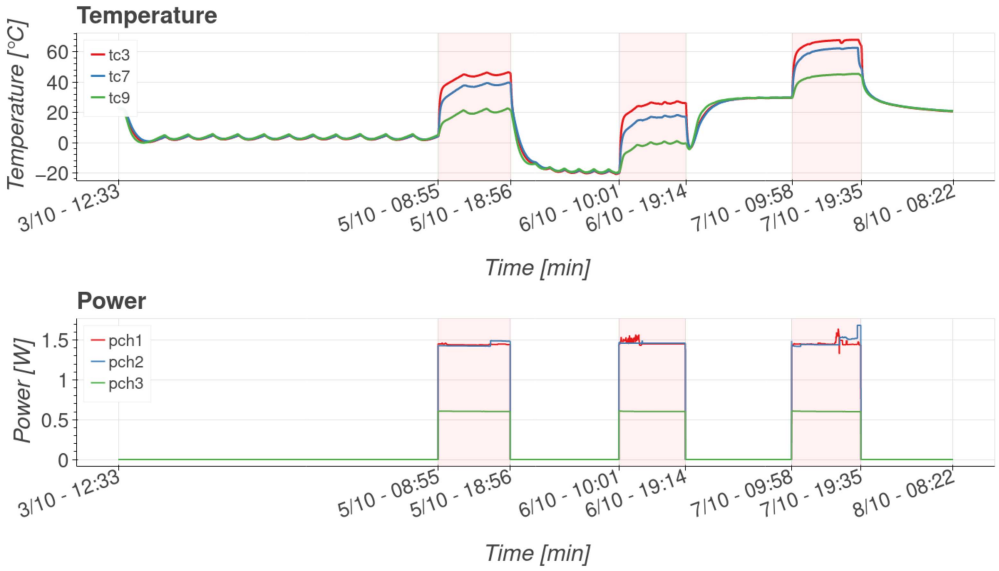

Figure 13. Heated internal boards temperatures and power. Inside the pale red bands heaters are on.

A quantitative view of the temperature jumps caused by the heaters heat dissipation—simulating the actual electronic heat dissipation—is shown in Figure 14. It is possible to verify how the 1.4 W delivered to PSU-PCB causes an increase of 44 °C on the board, and a corresponding increase of 20 °C in the crystal box.

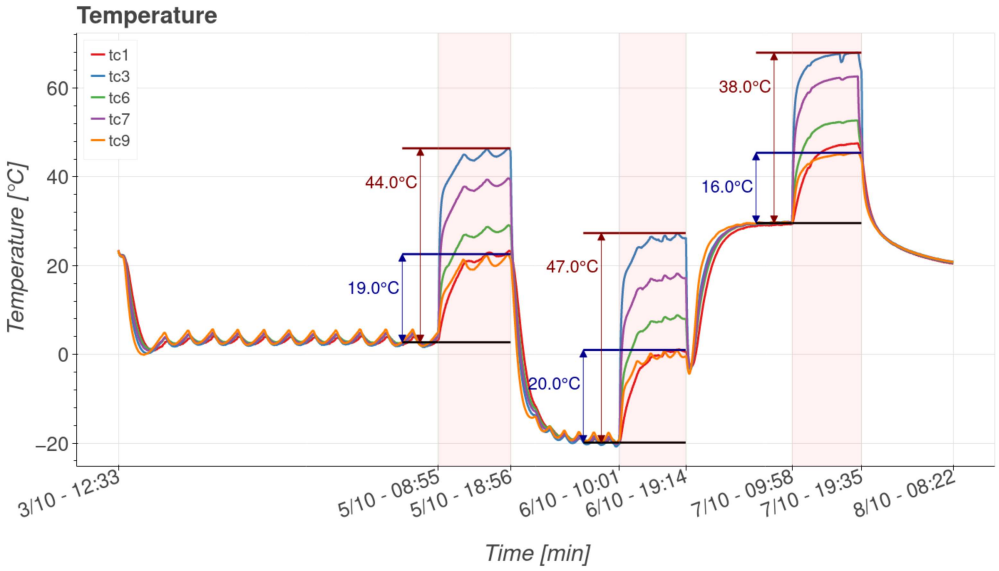

Figure 14. Temperature differences caused by heaters. Inside the pale red bands heaters are on.

The gradient of the boards temperature has been computed to verify the actual time needed to reach steady-state. In particular, the average gradient over a sliding window of the last 3 h has been monitored, and steady-state declared when its value stays below 0.01 °C min^{-1} for more than 1 h. Figure 15 reports the time to reach steady-state, computed as described. It is possible to observe how tc1 gradient is always below 1 °C min^{-1} as imposed by the test procedures to minimize thermo-mechanical stresses in the detectors. Furthermore, the maximum time needed to reach steady-state is registered by tc1 confirming the assumption made in Section 3.3.

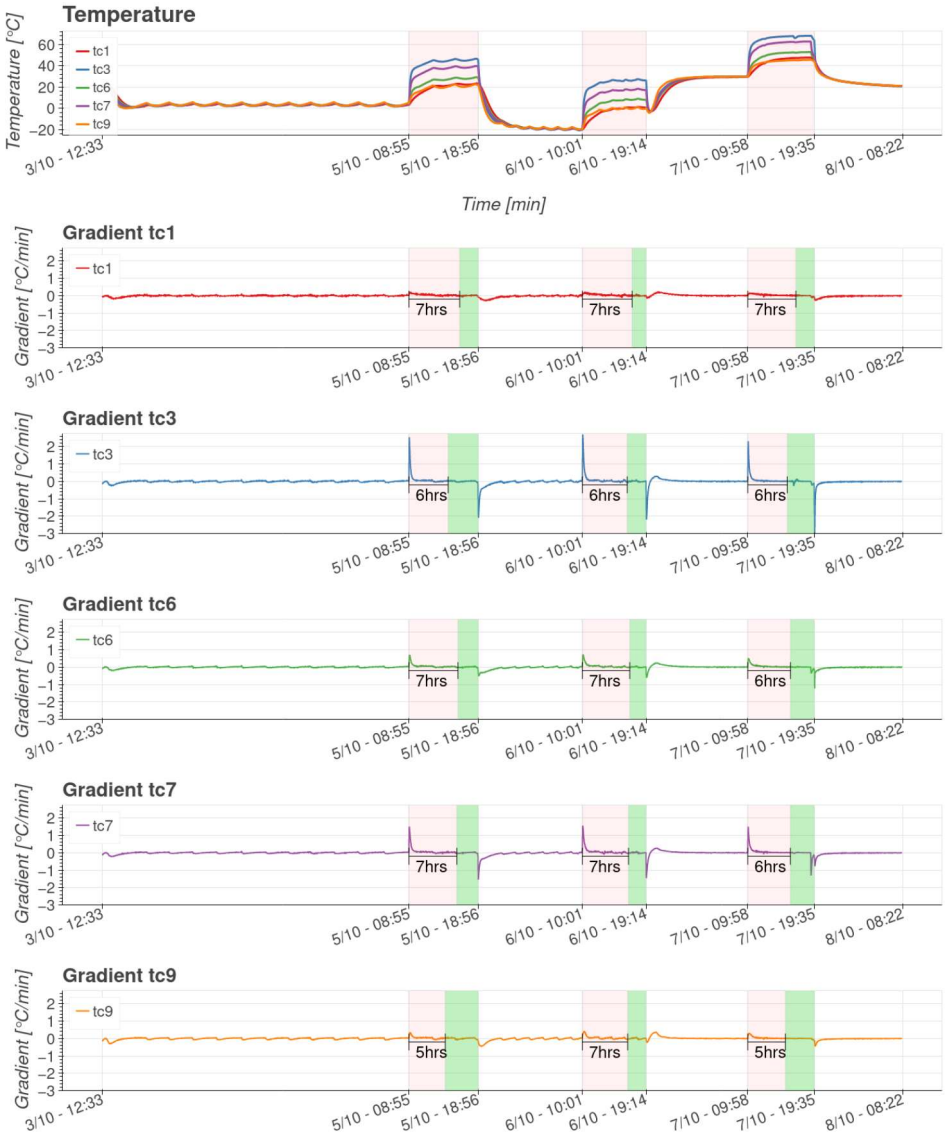

Figure 15. Payload internal components temperature gradients. Inside the pale red bands heaters are on.

The gradient analysis is also helpful to analyze the failure behaviour of tc12 compared to its redundant sensor tc17 (Figure 16). The TVAC temperature oscillations caused by the control action are not sudden due to the large mass of the baseplate, thus they do not justify the gradient spikes of tc12. Finally, the gradient analysis is also useful for Fault Detection Identification and Recovery (FDIR) either on board the CubeSat or by telemetry analysis on ground. Data can be exploited as footprint to spot TC failures on those components that have no redundancy on sensors for the temperature monitoring. Plus, the failure of tc12 confirms the necessity of such redundancy whenever monitoring a boundary condition during the TBT. As explained in Section 3.2, a failed acquisition of the temperature BCs would lead to a wrong model of the test environment, jeopardizing the thermal model correlation.

In conclusion, auto-correlation matrices including all TCs have been computed for time intervals in which the temperature at the interface between payload and TVAC has been changed, that is whenever a new set point has been asked to the controller. Auto-correlation was performed by computing the Pearson's coefficient between each measure point and all others for a time interval of 6 h starting whenever a new set point is targeted by the TVAC controller. The goal was to observe the degree of correlation between each TC

and the others to obtain a qualitative feeling about how temperature changes occurring in one measure point affect the other parts of the system, with a particular focus on how temperature changes at the DM interface with the TVAC affect the internal components of the payload. The DM TVAC interface is representative of the SM interface in the actual 3U CubeSat. Thus, by observing that region, it is possible to observe whether SM temperature variations will affect the temperature of the payload components. Auto-correlation matrices for internal and structural components are reported in Figure 17, and discussed in the following section.

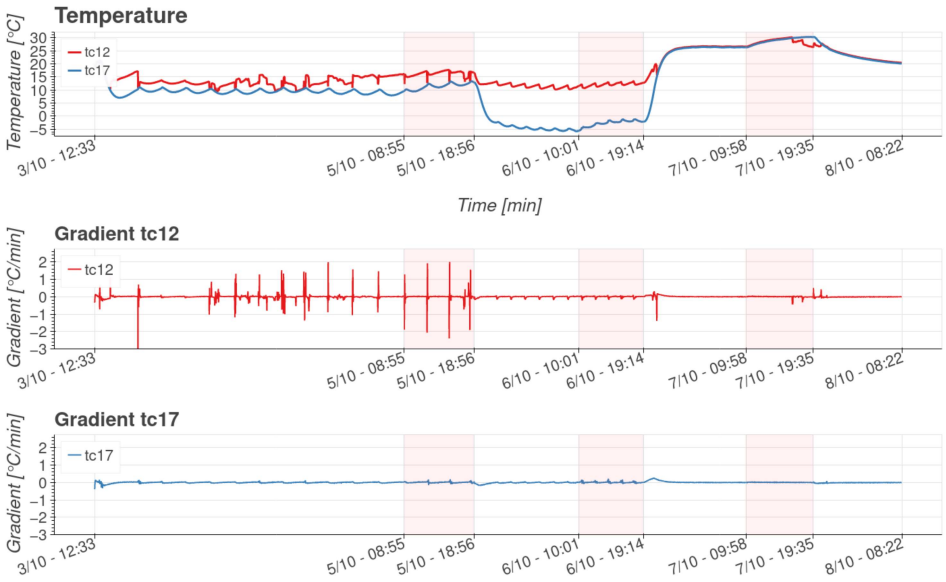

Figure 16. Broken TC12 behaviour compared to its redundant TC17.

A numerical overview of the test is given in Table 5: the table summarises all steady-state temperature values according to the three different set points with heaters both on and off. The value reported in each table cell refers to the mean over the last hour before the heaters are switched on and before they are switched off so the two steady-states at each set point before and after switching on the heaters are shown.

Table 5. Steady-state temperatures [°C] heaters off-on.

Component	TC	0 °C			−25 °C			30 °C		
		Off	On	Δ T	Off	On	Δ T	Off	On	Δ T
Crystal Box	tc1	2.65	22.91	20.26	−19.86	0.83	20.69	29.31	46.99	17.68
PSU	tc3	3.24	46.02	42.78	−20.37	26.42	46.79	29.61	66.93	37.32
FEE	tc6	3.42	28.71	25.29	−19.58	8.19	27.76	29.81	50.81	21.01
BEE FPGA	tc7	3.41	39.25	35.84	−19.84	17.41	37.25	29.82	57.67	27.85
PDHU	tc9	4.10	22.02	17.92	−19.58	−0.36	19.22	29.69	45.12	15.43
TVAC Interface	tc5	4.32	3.36	−0.95	−23.98	−24.32	−0.34	30.46	31.28	0.82
Rib +z −y	tc8	4.86	14.09	9.23	−18.42	−8.6	9.82	29.3	37.18	7.88
+x Panel	tc10	4.54	13.06	8.52	−19.85	−10.85	9.00	29.41	36.86	7.45
+y Panel	tc11	4.82	12.83	8.01	−18.91	−10.43	8.48	29.11	36.24	7.13
−x Panel	tc13	4.79	13.56	8.77	−18.87	−9.49	9.38	29.18	36.7	7.52
Rail +y +x	tc14	5.47	11.07	5.6	−17.67	−11.75	5.92	28.89	34.17	5.28
Rail +y −x	tc15	5.12	10.93	5.81	−18.68	−12.38	6.31	28.94	34.32	5.37
+y Shroud panel 1	tc12	15.93	15.95	0.01	10.99	12.36	1.37	26.61	26.68	0.08
TVAC Base Plate 1	tc16	4.52	2.68	−1.84	−23.03	−23.83	−0.8	29.67	30.3	0.62
+y Shroud panel 2	tc17	8.92	12.91	4.00	−5.58	−1.93	3.65	26.32	30.24	3.92
TVAC Base Plate 2	tc18	4.43	3.03	−1.39	−22.86	−23.52	−0.66	29.52	30.14	0.62
Top shroud 1	tc19	9.54	13.40	3.86	−3.9	−0.38	3.52	25.83	29.79	3.95
Top shroud 2	tc20	9.32	13.25	3.93	−4.24	−0.65	3.59	25.75	29.75	4.00

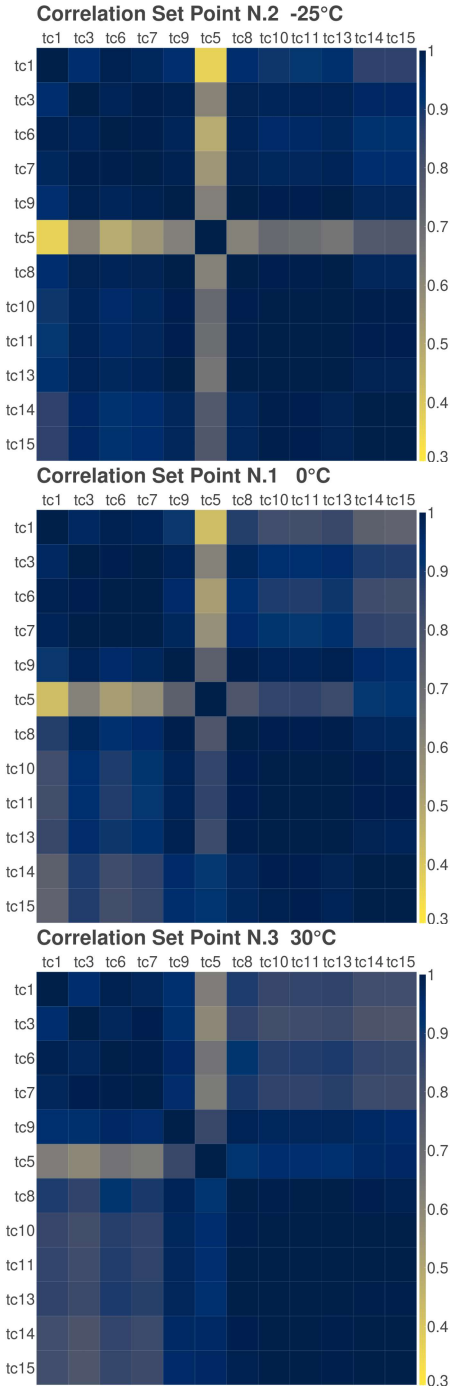

Figure 17. Autocorrelation matrices at set points. If one TC influences others the color is blue, otherwise yellow.

5. OpenFOAM FVTM Comparison

In this section the test results are compared with the FVTM built using the OpenFOAM code. The code has been selected because it is able to deal with complex geometries and maintain the geometrical accuracy. Furthermore, the contact interfaces are directly extracted from the geometry which avoids any simplification in the contact area definition, leading to more accurate results [7]. Moreover, the contact interface setup is fully automated and the code has already been numerically tested and compared against ESATAN for such type of application [7,42]. Thus, the comparison with experimental data is an added good proof for the use of the code in such scenarios and its future developments in the field [10–13]. Since the hot control of the TVAC guarantees small temperature oscillations in steady-state

it has been decided to perform the comparison at set point 30 °C. This enabled to run the simulation of the FVTM with a steady-state solver. In the cold cases, given the oscillations at the BCs a transient solver would have been necessary thus increasing the computational effort and time needed to run simulations. Furthermore, data comparison requires many runs of the simulation with variables changes thus the steady-state solver being faster helps reducing the overall computational time. The team is working on the complete transient analysis and it is left as the next research outcome.

5.1. Geometry and Materials

The geometry used for the FVTM is identical to the one provided by INAF except for three aspects. First, the connectors are simplified as the thermal resistance at the pins is not known. It would be pointless to use many cells to recreate the exact geometry if in the end the region is still full of uncertainties. Second, the geometries of the heaters and dummies are reproduced to have perfect correspondence with the test components as shown in Figure 18. Third, given the high number of parts in the simulations the crystal boxes have been clustered in order to reduce their number (Figure 19). They are not expected to have big temperature gradients nor they are critical from a thermal point of view.

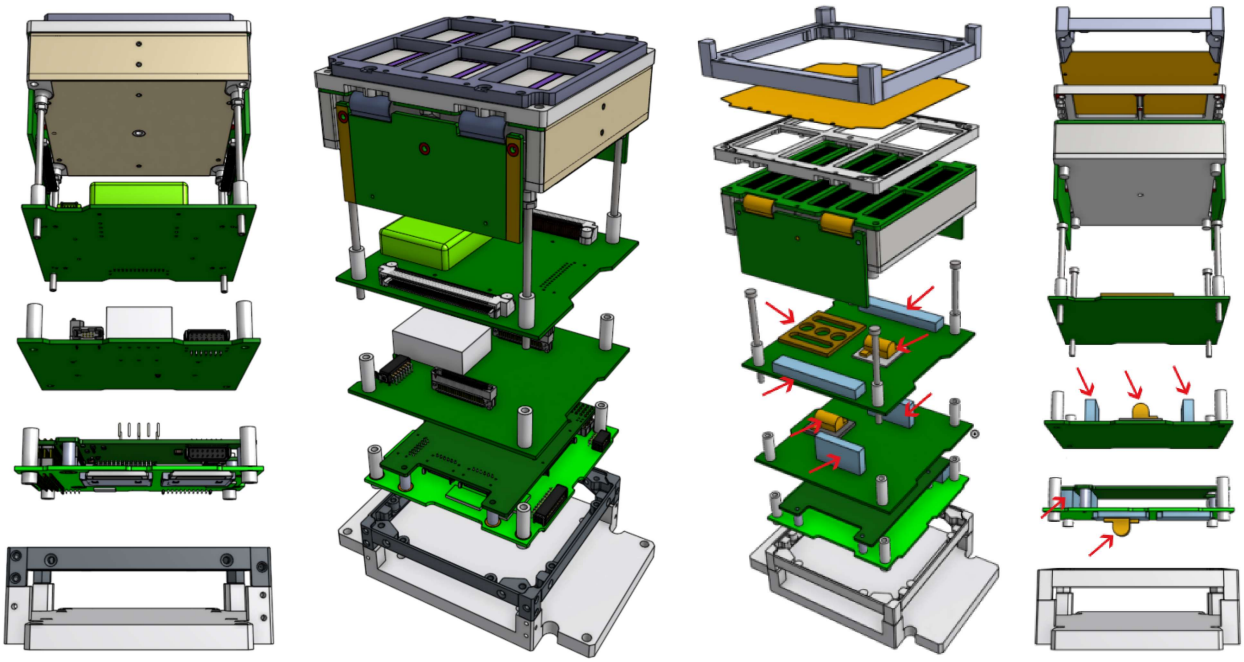

(**a**) INAF CAD (**b**) INAF CAD (**c**) Simulation geometry (**d**) Simulation geometry

Figure 18. Actual geometry of the DM (**a**,**b**). Geometry used in the simulation with connectors geometry simplified (**c**,**d**).

The total number of geometrical elements considered is 126. The corresponding number of cells, resulting from a grid sensitivity analysis, is 1.2 million cells and the mesh is pictured in Figure 20. All the interfaces between the regions that are in contact with each other in the geometry of the payload are extracted and considered in the simulation [7]. The number of geometrical interfaces is 458 for a total number of 1.4 million faces. The complexity of the geometry and the number of elements are a good test for the novel application of the finite volume method (FVM) in space thermal analysis.

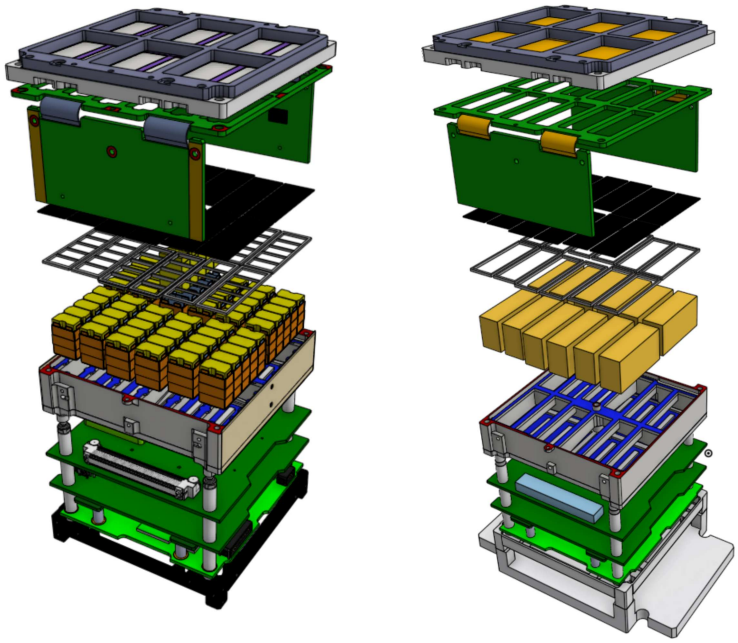

(**a**) INAF CAD (**b**) Simulation geometry

Figure 19. Actual geometry of the DM (**a**). Geometry used in the simulation with connectors geometry simplified (**b**).

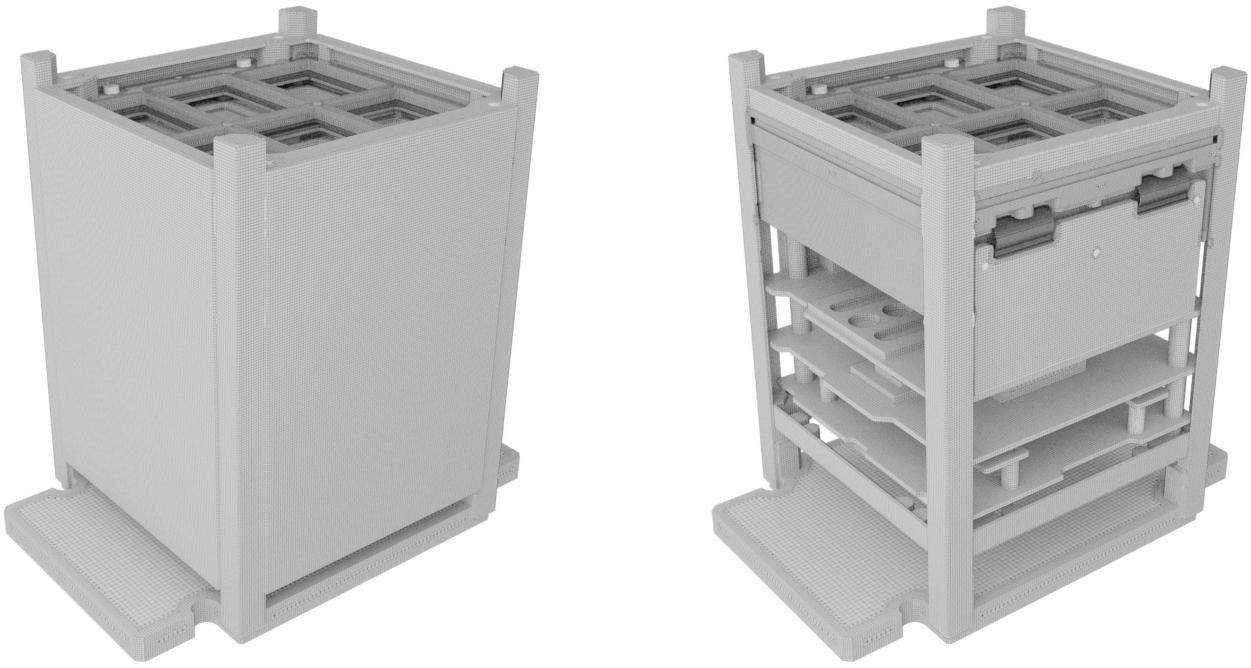

(**a**) Mesh structure (**b**) Mesh internal

Figure 20. Geometrical high detail accuracy mesh.

The materials used for the model are reported in Table 6. Given the low thickness of the PCB boards and the predominance of contact area and thermal contact conductance in the thermal heat exchange in vacuum conditions, the boards are assumed isotropic. The connection between the FEE lateral boards and the top board is made of copper strips as reported in the aforementioned table. For the structure, the rails have a black anodization

with a different emissivity value with respect to the polished aluminium used for the base plate and the other structural components. The emissivity value for the black anodization is given by the manufacturer and it is reported in the table. The emissivity of the interior side of the radiation shield is taken as the emissivity of a second surface mirror with Kapton thickness of 127 µm (http://www.sheldahl.com/sites/default/files/Documents/ShieldingMaterials/RedBook.pdf (accessed on 2 November 2022)) (5 mil).

Table 6. Material properties used in the simulation.

Material	ε_{IR}	k [W m^{-1} K^{-1}]	c_p [J kg^{-1} K^{-1}]	ρ [kg m^{-3}]
Structure (black coating)	0.86	220	910	2700
Structure, heaters, dummies	0.03	220	910	2700
PCB	0.80	20	560	2200
Connector	0.90	30	560	2200
FEE copper strips	0.03	400	385	8900
Radiation shield + Kapton	0.81	-	-	-

5.2. Boundary Conditions (BC)

As stated in Section 3.2, in order to reproduce the test radiative environment in the numerical simulation, a radiation shield has been placed around the payload. In this way, by knowing the temperatures at the walls of the shield through the TCs and the known emissivity of the Kapton placed inside it, is possible to properly set the BC of the simulation.

The BC of the numerical model are set according to the experimental values from the thermocouples, as reported in Figure 21. With the same approach used for the walls, the temperature BC of the aluminum base is determined. As reported in Section 3.2, it is assumed that the side panels of the shield have the same temperature, except for the top that is not bolted to the others. In any case, as reported in Table 5, the temperature difference between base plate and shield panels is less than 1 °C which is below the TC accuracy.

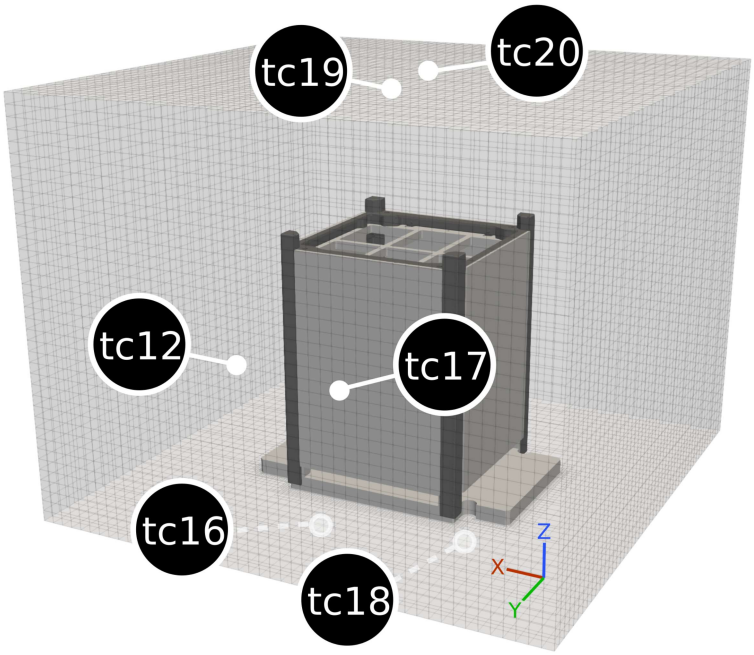

Figure 21. Simulation domain. Pale gray walls represent the shroud around the DM.

The description of the numerical schemes, the view factors calculation and the numerical setup is described in detail in [7], to which the interested reader is referred.

5.3. Comparison

The numerical temperature values are taken at the same positions of the thermocouples (Figure 22) and the comparison with test data is reported in Figure 23.

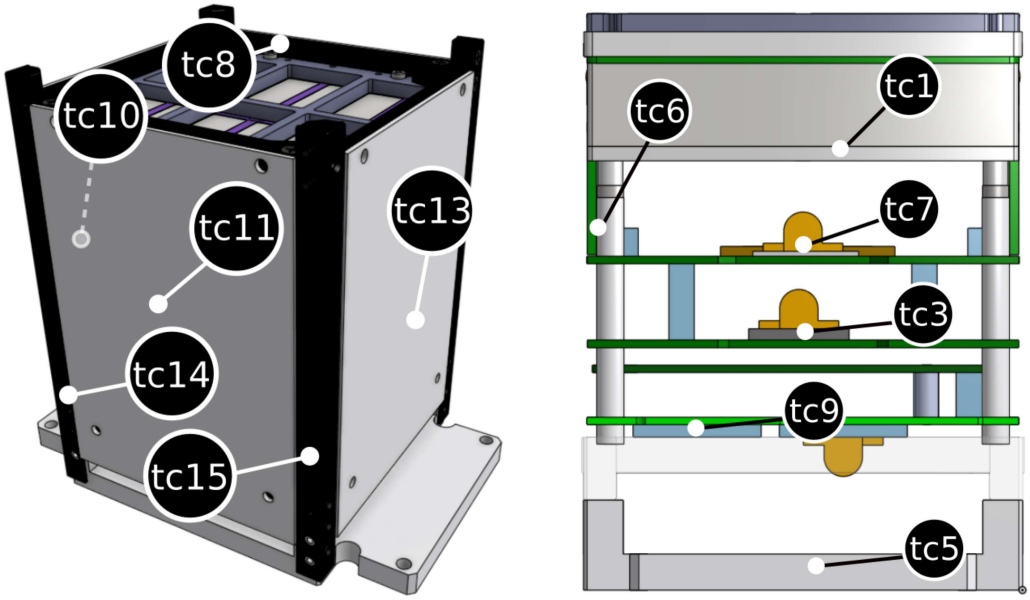

(**a**) TCs locations on the structure components (**b**) TCs locations on internal components

Figure 22. Thermocouple positions showed in the FVTM.

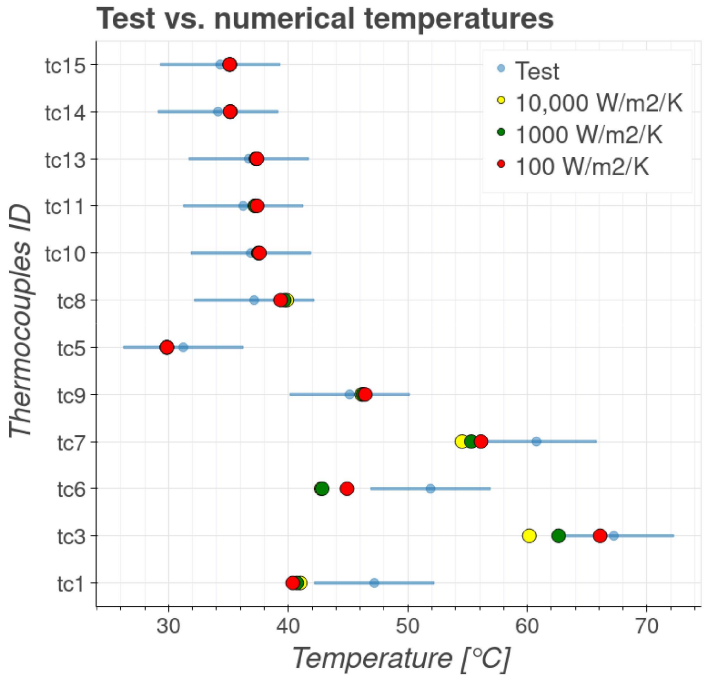

Figure 23. Numerical and test data comparison. Horizontal light blue line represents ±5 °C interval imposed by ECSS for correlation.

Since the HERMES program is a CubeSat mission, it is not forced to follow the ECSS space standards entirely, indeed a tailored version of such standards is used in CubeSat scenarios [4], nonetheless the team philosophy aims at following the ECSS standards as far as it is possible, thus the test data is compared to the FVTM results with the goal to reach the correlation standards of ECSS-E-ST-31C 4.5.3.3.c [3], for which the model is correlated if

the predicted temperature falls within ±5 °C from the test value. Indeed, from Figure 23 it is possible to observe that there is a very good correlation with the test results for all thermocouples placed on structural parts. This proves that FVTM is able to correctly predict the actual temperatures.

For the TCs on the internal components, the correlation is still good as reported in Figure 23 but some thermocouples are just at the boundary whilst others are a few degrees away from correlation, in particular tc1 and tc6 are out of the correlation criteria. It must be noted that the uppermost part of the payload, marked with tc8, and all the other internal thermocouples on the boards and structure are within correlation, thus the reason for this discrepancy cannot be caused by those regions. The cause of the divergence with high probability lies in the thermal connections inside the crystal box and in the sandwich assembly connecting it with the FEE and the components above the FEE (Figure 2). As reported in [20], the elements in that region of the payload are connected with a series of pads for the crystals and glues for the SDDs. All that complexity in the connections leads to a high grade of uncertainty in the actual thermal contact coefficient (see next section) between the elements causing with high probability the divergence. To better investigate the phenomena, a dedicated test shall be performed with a dedicated number of sensors in that region. Unfortunately, it is not possible to place any thermocouple in that region, for example upon the FEE close to SDDs or inside the crystal box. As pictured and reported in [20] there is no space where to place thermal sensors (plus the routing) upon the FEE or inside the crystal box, indeed all the thermocouples in the flight model for the payload unit are placed on the lateral panels. Given the impossibility to place sensors in the region and obtain the dedicated data on the thermal connections needed to update the FVTM, the team has decided to accept the divergence in the comparison with model results. Nonetheless, further analyses on this point are undergoing and will be presented in the next research outcomes.

5.4. Sensitivity Analysis on Spacer Contact Interfaces

The conductive interfaces are the ones that have the most impact on the temperature of the components [7,43,44], indeed the sensitivity analysis is performed on the contact interfaces of the internal components to push their temperature closer to the experimental one. All the boards in the stack are in contact through a set of spacers, thus the thermal contact coefficient between the spacers and the boards is modified in order to reach a better correlation. Such value is changed for all the spacers at once, indeed all the spacers have the same contact area with the boards and are mounted in a stack configuration (they are tightened axially), thus the pressure at those interfaces is equal. Since the spacers are made of the same material, they have the same surface roughness values. On the board side, there is an exposed conductive area around each mounting hole to guarantee the electrical connection with all the ground layers throughout all the electronics (Figure 6), so also in this case there is the same surface roughness value. In conclusion, the spacers' contact interfaces have the same pressure and same surface roughness, being these are the factors which influence the thermal contact coefficient, it is assumed that all those interfaces have the same thermal contact coefficient. The value has been changed from 10,000 $W\,m^{-2}\,K^{-1}$ to 100 $W\,m^{-2}\,K^{-1}$ with the latter resulting as the most accurate. The starting value of the contact coefficient is taken from a CubeSat stack dedicated test campaign [44], the last one is the reference conservative value for a low pressure contact between two aluminum interfaces [45]. The results are presented in Figure 23 and discussed in the next section.

It must be noted that the most responsive component is the middle board, i.e., the PSU, while the TCs on the upper part are quite insensitive to such changes. With high probability the thermal dynamics of the upper part (i.e., tc6 and tc1) is dominated by the links inside the detector. Unfortunately, there are no TCs inside the detector thus without data in that region it is not possible to investigate possible correlations.

5.5. Results

From the results of the FVTM it is clear that the PSU it the hottest board inside the payload as reported in Figure 24a. Furthermore, it is possible to observe how heat flows into the upper region of the payload Figure 24b from the BEE-PCB through the FEE-PCB towards the upper detector region.

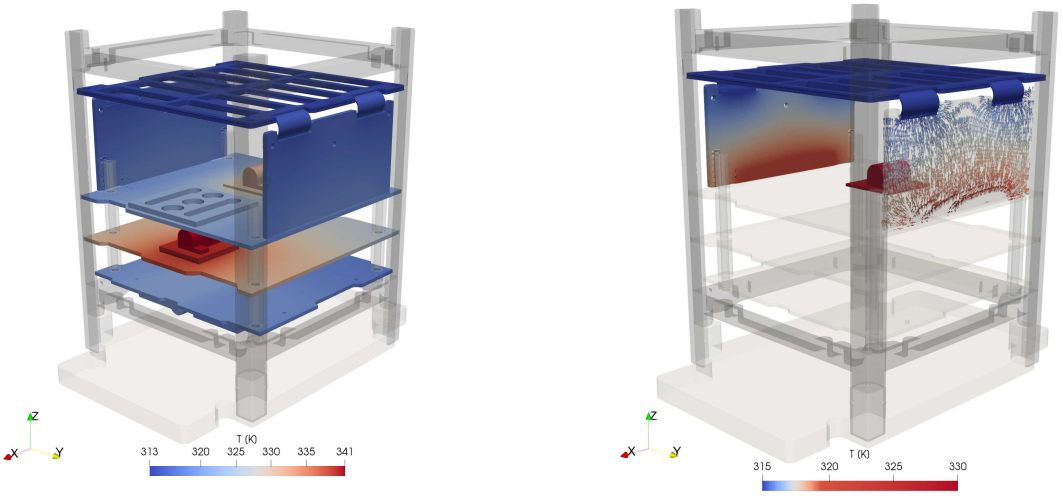

(**a**) (**b**)

Figure 24. FVTM temperature field results. Crystal box and other elements are not included to ease the visibility of interested regions. (**a**) FVTM temperature field. (**b**) Heat flow path visualization (normal vectors to isothermal lines).

The visualization of the heat flow path from the electronic boards towards the SDD tiles provides useful information about how to deviate such heat flux to keep the SDD temperature below the maximum value, i.e., −5 °C. The solution implemented by INAF is to provide exposed areas of the ground layers on the BEE-PCB and PSU-PCB, on which conductive spacers dissipators are placed as shown in Figure 25. The spacers will be linked with the lateral panels, acting as external radiators, through the SIL-PD TSP 3500 thermal conductive pad, thus creating a thermal interface. Moreover, the PL designers also decided to expose part of the ground layer on the FEE lateral wings, and to thermally connect it to the lateral panels by means of a thermal pad.

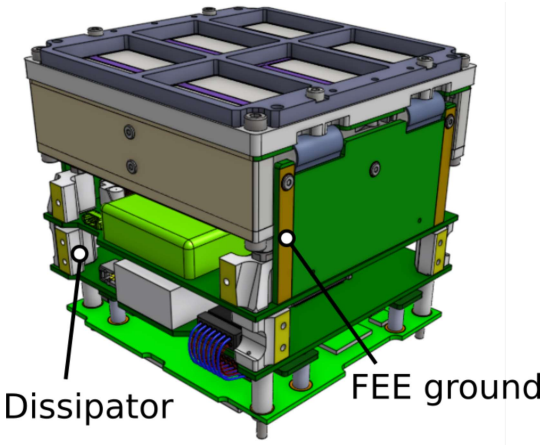

Figure 25. New thermal links regions with lateral panels. Modified spacers named as Dissipators in the picture and exposed ground layer on FEE.

The validation of the FVTM model is limited by the fact that the comparison is performed for a single steady state case, nonetheless, it is an important step to check the validity of the model. As stated in ECSS-E-ST-31C-4.5.3.3, the test data must be correlated both in steady state modes and transient modes, so the presented work satisfies only a part of the standards, the team is now validating the transient case. Once the model is validated, the team will be able to quantify the effects on the temperature field of the newly designed spacers used as thermal links with the payload panels without performing test campaigns. This will enable the team to check if other modifications to the spacers and their connections are necessary to lower the detector temperature.

6. Discussion

The thermal test performed on the payload DM produced sufficient data to move into the steady-state correlation with the FVTM. Apart from the steady-state temperatures, the test highlighted other important results, briefly summarised hereafter.

First, the time to reach steady-state in a laboratory size TVAC has been established: this is important for future AIT/AIV activities adequate planning. Usually, the nominal approach is to create the numerical setup of the test and have an estimation of the transient time. In our case, having access to the TVAC and the DM in the design phase, it was faster to jump straight into testing, gathering all the data and then move into the numerical simulation for the FVTM.

As a second result, the temperature increase in the boards caused by the heaters power dissipation has been analyzed: those are crucial data to refine the thermal control subsystem design for the HERMES satellite, as they give an actual measure of the temperature increase that the boards might experience whenever turned on. Furthermore, it allows to properly choose the set point temperatures in future tests in order to avoid the overshooting of the upper temperature limits of the boards whenever turned on.

Third, and probably the most important, the auto-correlation matrices show that the TC at the payload interface with the TVAC (tc5) is weakly correlated with the thermocouples placed on the internal components of the payload. Figure 17 clearly shows this aspect: the red rectangle highlights the cells correlating tc5 with the TCs on the boards inside the PL (i.e., tc1–tc9). It means that temperature changes at the interface between the payload and the TVAC slightly affect the components inside the payload. This is good news in terms of thermal control complexity relaxation, as it means that once the flight segment is fully integrated, the SM temperature has little impact on the payload components leaving the PL and SM thermal behaviour substantially decoupled. Please note that Pearson's coefficient is influenced by the time delay between each temperature data but overall the qualitative results are not much influenced.

Fourth, it is possible to observe from the auto-correlation matrices in Figure 17 how the correlation between tc5 (interface with TVAC) and the internal components increases with temperature. An explanation for such phenomena might be due to the fact that thermal contact resistance usually decreases as the temperature increases, thus the components are able to exchange bigger heat fluxes hence the correlation increases. Unfortunately, there is scarce literature that analyzes this phenomenon at ambient temperature but for higher temperatures and cryogenic ones such behaviour is confirmed [46,47]. The behaviour might be confirmed from Table 5, especially on the PSU where the temperature jump ΔT caused by the power on of the board is smaller in the hot cycle with respect to the cold ones, meaning that more heat has been dissipated towards other components due to the smaller contact resistance hence the lower temperature jump. For the PSU the temperature jump at $-25\,^{\circ}C$ is around 47 degrees whilst at $30\,^{\circ}C$ is around 37 degrees, thus the phenomenon has a relevant impact on the temperature field. In any case, to fully confirm such phenomena, a dedicated test must be performed, an example is given in [44].

On the other hand, a slight, opposite behaviour is observed on all TCs placed on the structural components (i.e., tc8–tc15 in Figure 17). This behaviour still remains an open point. Data gathered with the presented set up do not suffice to further investigate the case,

thus a dedicated test is needed to understand this phenomenon. In any case, since no major effect on the payload components has been observed due to this behavior, it is assumed not to represent a critical issue.

As a final point, the FVTM is compared with the hot steady-state values. For what concerns the structural components, there is a perfect match between the numerical data and the test results. There is a good match with the internal components and the reason of the difference is explained in Section 5.3.

Finally, the presented results agree with analogous activities carried out on flying CubeSats: for instance, the temperature discrepancies between numerical and experimental results found in [5] are compatible with the outcome of the present work.

7. Conclusions

The thermal balance test and test setup procedure for the HERMES CubeSat Payload DM have been presented and the conclusions are here summarized:

1. the gathered data highlight the time needed to reach steady-state, the temperature jumps caused by the simulated electronic heat power dissipation and showed how the internal components of the payload DM are not much affected by the temperature changes at the interface with the rest of the spacecraft.
2. the test showed the actual thermal behaviour of the payload pushing the payload team to modify the thermal design. Indeed, new thermal interfaces have been introduced and strategically placed to deviate heat flux from flowing towards the detectors which must be kept below $-5\,^{\circ}C$ during the operations.
3. the novel application of FVM proved to be suitable for thermal analyses on space systems as it correctly predicted the payload thermal behaviour. The FVTM is compared with the test data presented in the article and its application can now be extended to other cases. The flexibility and high level of detail offered by the method make its application promising to analyze other case scenarios such as asteroids and space debris, as demonstrated in [10,11].

As previously mentioned, the future developments consist of the complete transient thermal analysis to perform a comprehensive correlation of the thermal model.

Author Contributions: Conceptualization, all authors; methodology, M.Q., G.S., R.P., F.F. (Fabio Fuschino), Y.E., G.M., S.S., M.G. and L.M.; software, M.Q. and G.M.; validation, M.Q., G.M., M.G. and L.M.; formal analysis, M.Q., G.M., M.G., L.M., R.P., and Y.E.; investigation, M.Q., G.S., R.P., F.F. (Fabio Fuschino), Y.E. and G.M.; resources, R.P., F.F. (Fabio Fuschino), Y.E., G.M., F.F. (Fabrizio Fiore) and M.L.; data curation, M.Q., G.S., R.P., F.F. (Fabio Fuschino); writing—original draft preparation, M.Q.; writing—review and editing, all authors; visualization, M.Q.; supervision, R.P., F.F. (Fabio Fuschino), Y.E., G.M., S.S., F.F. (Fabrizio Fiore) and M.L.; project administration, Y.E., F.F. (Fabrizio Fiore) and M.L.; funding acquisition, Y.E., F.F. (Fabrizio Fiore) and M.L. All authors have read and agreed to the published version of the manuscript.

Funding: This research was funded by ASI Grant n.2018-13-HH.0, "HERMES TP-Attività di Sistema" and by ASI Grant n.2018-10-HH.0. The work is done under the H2020 space programme framework with the Grant n.821896—HERMES-SP.

Institutional Review Board Statement: Not applicable.

Informed Consent Statement: Not applicable.

Acknowledgments: The authors thanks the staff of the Experimental Test Laboratory of the Department of Aerospace Science and Technology of Politecnico di Milano for the help in the test preparation and activities. Special thanks to Federico Piscaglia for the help in the set up of the server machines on CFDHub and thanks to Paolo Lunghi for reviewing the article.

Conflicts of Interest: The authors declare no conflict of interest.

Abbreviations

The following abbreviations are used in this manuscript:

BC	Boundary Condition
BEE	Back End Electronics
CFD	Computational Fluid Dynamics
DM	Demonstration Model
ECSS	European Cooperation for Space Standardization
FDIR	Fault Detection Identification and Recovery
FEE	Front End Electronics
FM	Flight Model
FPGA	Field Programmable Gate Array
FVM	Finite Volume Method
FVTM	Finite Volume Thermal Model
GCN	Gamma-Rays Coordinated Network
GPS	Global Positioning System
GRB	Gamma Ray Burst
INAF	Istituto Nazionale di Astrofisica
LPA	Lumped Parameter Approach
PCB	Printed Circuit Board
PCH	Power Channel
PDHU	Payload Data Handling Unit
PL	Payload
PSU	Power Supply Unit
SDD	Silicon Drift Detector
SM	Service Module
TC	Thermocouple
TVAC	Thermal Vacuum Chamber

References

1. Fiore, F.; Burderi, L.; Lavagna, M.; Bertacin, R.; Evangelista, Y.; Campana, R.; Fuschino, F.; Lunghi, P.; Monge, A.; Negri, B.; et al. The HERMES-technologic and scientific pathfinder. In Proceedings of the Space Telescopes and Instrumentation 2020: Ultraviolet to Gamma Ray, Online, 14–22 December 2020; SPIE: Bellingham, WA, USA, 2020; Volume 11444, pp. 214–228. . [CrossRef]
2. Scala, F.; Zanotti, G.; Curzel, S.; Fetescu, M.; Lunghi, P.; Lavagna, M.; Lavagna, M.; Bertacin, R. The HERMES mission: A CubeSat constellation for multi-messenger astrophysics. In Proceedings of the 5th IAA Conference on University Satellite Missions and CubeSat Workshop, Rome, Italy, 28–30 January 2020; pp. 1–17.
3. European Cooperation for Space Standardization. ECSS-E-ST-31C—Thermal Control (15 November 2008). Available online: https://ecss.nl/standard/ecss-e-st-31c-thermal-control/ (accessed on 2 November 2022).
4. European Cooperation for Space Standardization. Tailored ECSS for IOD CubeSats. 2016. Available online: https://copernicus-masters.com/wp-content/uploads/2017/03/IOD_CubeSat_ECSS_Eng_Tailoring_Iss1_Rev3.pdf (accessed on 2 November 2022).
5. Mason, J.P.; Lamprecht, B.; Woods, T.N.; Downs, C. CubeSat on-orbit temperature comparison to thermal-balance-tuned-model predictions. *J. Thermophys. Heat Transf.* **2018**, *32*, 237–255.
6. Dunwoody, R.; Reilly, J.; Murphy, D.; Doyle, M.; Thompson, J.; Finneran, G.; Salmon, L.; O'Toole, C.; Reddy Akarapu, S.K.; Erkal, J.; et al. Thermal Vacuum Test Campaign of the EIRSAT-1 Engineering Qualification Model. *Aerospace* **2022**, *9*, 99.
7. Quirino, M.; Marocco, L.; Guilizzoni, M.; Lavagna, M. High Energy Rapid Modular Ensemble of Satellites Payload Thermal Analysis Using OpenFOAM. *J. Thermophys. Heat Transfer* **2021**, *35*, 4.
8. Morsch Filho, E.; Seman, L.O.; Paulo Nicolau, V.d. Simulation of a CubeSat with internal heat transfer using Finite Volume Method. *Appl. Therm. Eng.* **2021**, *193*, 117039. [CrossRef]
9. Das, R.; Mishra, S.C.; Ajith, M.; Uppaluri, R. An inverse analysis of a transient 2-D conduction–radiation problem using the lattice Boltzmann method and the finite volume method coupled with the genetic algorithm. *J. Quant. Spectrosc. Radiat. Transf.* **2008**, *109*, 2060–2077. [CrossRef]
10. Piccinin, M.; Civardi, G.L.; Quirino, M.; Lavagna, M. Multispectral Imaging Sensors for Asteroids Relative Navigation. In Proceedings of the International Astronautical Congress (IAC), Dubai, United Arab Emirates, 25–29 October 2021.
11. Civardi, G.L.; Bechini, M.; Colombo, A.; Quirino, M.; Piccinin, M.; Lavagna, M. VIS-TIR Imaging for Uncooperative Objects Proximity Navigation: A Tool for Development and Testing. In Proceedings of the 11th International Workshop on Satellite Constellations & Formation Flying, Milano, Italy, 7–10 June 2022.
12. Bechini, M.; Civardi, G.L.; Quirino, M.; Colombo, A.; Lavagna, M. Robust Monocular Pose Initialization via Visual and Thermal Image Fusion. In Proceedings of the 73rd International Astronautical Congress, Paris, France, 18–22 September 2022.

13. Colombo, A.; Civardi, G.L.; Bechini, M.; Quirino, M.; Lavagna, M. VIS-TIR cameras data fusion to enhance relative navigation during In Orbit Servicing operations. In Proceedings of the 73rd International Astronautical Congress, Paris, France, 18–22 September 2022.
14. Colagrossi, A.; Prinetto, J.; Silvestrini, S.; Lavagna, M.R. Sky visibility analysis for astrophysical data return maximization in HERMES constellation. *J. Astron. Telesc. Instrum. Syst.* **2020**, *6*, 048001.
15. Colagrossi, A.; Prinetto, J.; Silvestrini, S.; Orfano, M.; Lavagna, M.; Fiore, F.; Burderi, L.; Bertacin, R.; Pirrotta, s. Semi-Analytical Approach to Fasten Complex and Flexible Pointing Strategies Definition for Nanosatellite Clusters: The HERMES Mission Case from Design to Flight. In Proceedings of the 70th International Space Congress, Washington, DC, USA, 21–25 October 2019; pp. 1–20.
16. Cinelli, M.; Puccetti, S.; Lavagna, M.; Lunghi, P.; Pucacco, G. High Energy Modular Ensemble of Satellites Mission: Towards the final Full Constellation. *Acta Astronaut.* **2021**, *189*, 129–142. [CrossRef]
17. Fiore, F.; Burderi, L.; Salvo, T.D.; Feroci, M.; Labanti, C.; Lavagna, M.R.; Pirrotta, S. HERMES: A swarm of nano-satellites for high energy astrophysics and fundamental physics. In Proceedings of the Space Telescopes and Instrumentation 2018: Ultraviolet to Gamma Ray, Austin, TX, USA, 10–15 June 2018; SPIE: Bellingham, WA, USA, 2018; Volume 10699, p. 106992Q. [CrossRef]
18. Burderi, L.; Salvo, T.D.; Riggio, A.; Gambino, A.F.; Sanna, A.; Fiore, F.; Amarilli, F.; Amati, L.; Ambrosino, F.; Amelino-Camelia, G.; et al. GrailQuest and HERMES: Hunting for gravitational wave electromagnetic counterparts and probing space-time quantum foam. In Proceedings of the Space Telescopes and Instrumentation 2020: Ultraviolet to Gamma Ray, Online, 14–22 December 2020; SPIE: Bellingham, WA, USA, 2021; Volume 11444, pp. 863–881. [CrossRef]
19. Sanna, A.; Burderi, L.; Salvo, T.D.; Fiore, F.; Riggio, A.; Gambino, A.; Lavagna, M.; Bertacin, R.; Evangelista, Y.; Campana, R.; et al. Timing techniques applied to distributed modular high-energy astronomy: The H.E.R.M.E.S. project. In Proceedings of the Space Telescopes and Instrumentation 2020: Ultraviolet to Gamma Ray, Online, 14–22 December 2020; SPIE: Bellingham, WA, USA, 2020; Volume 11444, pp. 844–862. [CrossRef]
20. Evangelista, Y.; Fiore, F.; Fuschino, F.; Campana, R.; Ceraudo, F.; Demenev, E.; Guzman, A.; Labanti, C.; Rosa, G.L.; Fiorini, M.; et al. The scientific payload on-board the HERMES-TP and HERMES-SP CubeSat missions. In Proceedings of the Space Telescopes and Instrumentation 2020: Ultraviolet to Gamma Ray, Online, 14–22 December 2020; SPIE: Bellingham, WA, USA, 2020; Volume 11444, pp. 241–256. [CrossRef]
21. Fuschino, F.; Campana, R.; Labanti, C.; Evangelista, Y.; Fiore, F.; Gandola, M.; Grassi, M.; Mele, F.; Ambrosino, F.; Ceraudo, F.; et al. An innovative architecture for wide band transient monitor on board the HERMES nano-satellite constellation. In Proceedings of the Space Telescopes and Instrumentation 2020: Ultraviolet to Gamma Ray, Online, 14–22 December 2020; SPIE: Bellingham, WA, USA, 2020; Volume 11444, pp. 229–240. [CrossRef]
22. Dilillo, G.; Campana, R.; Zampa, N.; Fuschino, F.; Pauletta, G.; Rashevskaya, I.; Ambrosino, F.; Baruzzo, M.; Cauz, D.; Cirrincione, D.; et al. A summary on an investigation of GAGG:Ce afterglow emission in the context of future space applications within the HERMES nanosatellite mission. In Proceedings of the Space Telescopes and Instrumentation 2020: Ultraviolet to Gamma Ray, Online, 14–22 December 2020; SPIE: Bellingham, WA, USA, 2020; Volume 11444, pp. 1310–1317. [CrossRef]
23. Fuschino, F.; Campana, R.; Labanti, C.; Evangelista, Y.; Feroci, M.; Burderi, L.; Fiore, F.; Ambrosino, F.; Baldazzi, G.; Bellutti, P.; et al. HERMES: An Ultra-Wide Band X and Gamma-Ray Transient Monitor on Board a Nano-Satellite Constellation. *Nucl. Instrum. Methods Phys. Res. Sect. A Accel. Spectrometers Detect. Assoc. Equip.* **2019**, *936*, 199–203. [CrossRef]
24. Grassi, M.; Gandola, M.; Mele, F.; Bertuccio, G.; Malcovati, P.; Fuschino, F.; Campana, R.; Labanti, C.; Fiorini, M.; Evangelista, Y.; et al. X-/y-Ray Detection Instrument for the HERMES Nano-Satellites Based on SDDs Read-Out by the LYRA Mixed-Signal ASIC Chipset. In Proceedings of the 2020 IEEE International Instrumentation and Measurement Technology Conference (I2MTC), Dubrovnik, Croatia, 25–28 May 2020; pp. 1–6. [CrossRef]
25. Campana, R.; Fuschino, F.; Evangelista, Y.; Dilillo, G.; Fiore, F. The HERMES-TP/SP background and response simulations. In Proceedings of the Space Telescopes and Instrumentation 2020: Ultraviolet to Gamma Ray, Online, 14–22 December 2020; SPIE: Bellingham, WA, USA, 2020; Volume 11444, pp. 817–824. [CrossRef]
26. Galgoczi, G.; Ripa, J.; Dilillo, P.; Ohno, M.; Campana, R.; Werner, N. A software toolkit to simulate activation background for high energy detectors onboard satellites. In Proceedings of the Space Telescopes and Instrumentation 2020: Ultraviolet to Gamma Ray, Online, 14–22 December 2020; SPIE: Bellingham, WA, USA, 2020; Volume 11444, pp. 1300–1309. [CrossRef]
27. Řípa, J.; Dilillo, G.; Campana, R.; Galgóczi, G. A comparison of trapped particle models in low Earth orbit. In Proceedings of the Space Telescopes and Instrumentation 2020: Ultraviolet to Gamma Ray, Online, 14–22 December 2020; SPIE: Bellingham, WA, USA, 2020; Volume 11444, pp. 597–606. [CrossRef]
28. Microsemi. Chip Scale Atomic Clock (CSAC) | Microsemi. 2021. Available online: https://www.microsemi.com/product-directory/embedded-clocks-frequency-references/5207-space-csac (accessed on 2 November 2022).
29. Socomore. AEROGLAZE A276—Socomore. 2021. Available online: https://www.socomore.com/media/akeneo_connector/asset_files/a/e/aeroglaze_a276_TDS_english.pdf (accessed on 2 November 2022).
30. Baroni, A. Control Design of a Thermal Vacuum Chamber Cooling System Based on Artificial Neural Network. Master's Thesis, Politecnico di Milano, Milan, Italy, 2019. Available online: http://hdl.handle.net/10589/151646 (accessed on 2 November 2022).
31. Restelli, A. Neural Network Inverse-Model Control of Thermal Vacuum Chamber Temperature. Master's Thesis, Politecnico di Milano, Milan, Italy, 2018. Available online: http://hdl.handle.net/10589/140420 (accessed on 2 November 2022).

32. Tacca, S. Controllo Termico Predittivo di una Camera Termovuoto per Prove di Qualifica Spaziali. Master's Thesis, Politecnico di Milano, Milano, Italy, 2013. Available online: http://hdl.handle.net/10589/79813 (accessed on 2 November 2022).
33. Sciarrone, G. Test Termo-Meccanici sul Payload Demostration Model dell Missione Spaziale HERMES. Master's Thesis, Sapienza Università di Roma, Milan, Italy, 2021.
34. European Cooperation for Space Standardization. ECSS-E-ST-10-03C—Testing (1 June 2012). Available online: https://ecss.nl/standard/ecss-e-st-10-03c-rev-1-testing-31-may-2022/ (accessed on 2 November 2022).
35. Escobar, E.; Diaz, M.; Zagal, J.C. Evolutionary design of a satellite thermal control system: Real experiments for a CubeSat mission. *Appl. Therm. Eng.* **2016**, *105*, 490–500. [CrossRef]
36. Guzman, A.; Pliego, S.; Bayer, J.; Evangelista, Y.; La Rosa, G.; Sottile, G.; Curzel, S.; Campana, R.; Fiore, F.; Fuschino, F.; et al. The Payload Data Handling Unit (PDHU) on-board the HERMES-TP and HERMES-SP CubeSat Missions. *arXiv* **2021**, arXiv: 2101.03947.
37. Termocoppia tipo T, cavo 1m, Diametro Sonda 1/0.2 mm, Lunghezza Sonda 1m a +250 °C IEC | RS Components. 2021. Available online: https://it.rs-online.com/web/p/termocoppie/3630266 (accessed on 2 November 2022).
38. 34970A—Unità di acquisizione dati, mainframe a 3 ingressi, DMM 6,5 cifre, 240V, serie Keysight Switch Unit. 2021. Available online: https://it.farnell.com/keysight-technologies/34970a/data-acquisition-250-ch-sec-22/dp/1335867 (accessed on 2 November 2022).
39. 10 Watts Aluminium Housed Resistor | Heat Sink Resistor | Arcol Resistors | Aluminum Clad Resistors. 2021. Available online: https://www.ohmite.com/arcolresistors/hs-aluminum-housed/(accessed on 2 November 2022).
40. GPS-4303—Alimentazione da Banco, CC, Lineare, Regolabile, 4 Uscite, 0 V, 30 V, 0 A, 3 A. 2021. Available online: https://it.farnell.com/gw-instek/gps-4303/alimentazione-4-o-p-3a-30v-reg/dp/2748523 (accessed on 2 November 2022).
41. USB-6289. 2021. Available online: https://www.ni.com/it-it/support/model.usb-6289.html (accessed on 2 November 2022).
42. Quirino, M. Thermal Analysis of HERMES-TP CubeSat Using ESATAN and OpenFOAM. Master's Thesis, Politecnico di Milano, Milano, Italy, 2019. Available online: http://hdl.handle.net/10589/151674 (accessed on 2 November 2022).
43. Nijenhuis, A.K.t.; Brouwer, H.S.B.; Jonsson, M.; Bloem, E.A.; Benthem, R.C.v.; Volmuller, G.J. Thermal Modelling of CubeSats in ESATAN-TMS. In Proceedings of the 50th International Conference on Environmental Systems, Lisbon, Portugal, 31 July 2020. Available online: https://hdl.handle.net/2346/86456 (accessed on 2 November 2022).
44. Hager, P.B.; Flecht, T.; Janzer, K.; Brouwer, H.; Jonsson, M.; Pérez, L.L. Contact Conductance in Common CubeSat Stacks. In Proceedings of the 49th International Conference on Environmental Systems, Boston, MA, USA, 7–11 July 2019; p. 14. Available online: https://hdl.handle.net/2346/84563 (accessed on 2 November 2022).
45. Lienhard, J.H., IV; Lienhard V, J.H. *A Heat Transfer Textbook*, 5th ed.; Phlogiston Press: Cambridge, MA, USA, 2020. Available online: http://ahtt.mit.edu (accessed on 2 November 2022).
46. Bi, D.; Chen, H.; Ye, T. Influences of temperature and contact pressure on thermal contact resistance at interfaces at cryogenic temperatures. *Cryogenics* **2012**, *52*, 403–409. [CrossRef]
47. Dou, R.; Ge, T.; Liu, X.; Wen, Z. Effects of contact pressure, interface temperature, and surface roughness on thermal contact conductance between stainless steel surfaces under atmosphere condition. *Int. J. Heat Mass Transf.* **2016**, *94*, 156–163. [CrossRef]